



Università degli Studi del Sannio

DIPARTIMENTO DI INGEGNERIA

Corso di Laurea in Ingegneria Energetica

Tesi di Laurea

in

Fisica Generale

**Electromagnetic and Vacuum Properties of
Open Cell Conductive Foams for
Accelerators Rings**

Thesis Advisor:

Prof. Stefania Petracca

Author:

Emanuela Carideo

Co-Advisor:

Prof. Vincenzo Fiumara

Matr.864000147

Dott. Arturo Stabile

ACADEMIC YEAR 2013/2014

*“A colei che ha lottato fino alla fine...
mia madre...esempio di forza e coraggio..”*

Introduction

Molecular gas desorption from the beam pipe wall due to synchrotron radiation should be properly taken into account in the design of high-energy particle accelerators and storage rings. This has been a major (solved) challenge for the Large Hadron Collider, will be even more critical for the HE-LHC, in view of its higher level of synchrotron radiation, and will be a crucial issue for the successful operation of the proposed electron-positron Higgs factories.

The Open cell metal foams (OCMF) have been recently suggested as a possible alternative to perforated metal patches for efficiently handling gas desorption from the beam pipe wall in high synchrotron particle accelerators (such as the Large Hadron Collider-LHC at CERN), in view of its superior performance in terms of residual gas concentration and beam shielding.

In this thesis we discuss of the electromagnetic properties and the vacuum issues of the OMCFs, how they affect the beam coupling impedances, thanks to their surface roughness, and how they reduce the Secondary Electron Emission (SEY), thus alleviating the Electron Cloud (EC) build-up phenomenon and related instabilities.

Measurements with the **MU-EPSLN**TM were performed on Al and Cu foams in order to achieve reasonable numerical results for transmission and reflection coefficients in terms of permittivity (ϵ) and permeability (μ), to calculate impedances.

Table of Contents

Introduction	iii
Table of Contents	iv
1 Basic concepts of the Accelerators	1
1.1 Structure and uses of Accelerators	2
1.2 Luminosity of a High Energy Collider	4
1.3 Linear beam dynamics	6
1.3.1 Magnetic fields and transverse particle motion	8
1.3.2 Electric fields and longitudinal particle motion	12
1.3.3 Phase Stability of the bunched beam acceleration	16
2 Synchrotron Radiation	18
2.1 Radiation from Relativistic Particles	19
2.2 Damping of Oscillations	23
3 Wake fields and Impedance	28
3.1 Debye Potentials	28
3.2 Coupling Impedances, Debye Potentials and Parasitic Loss	30
3.3 Perturbative Formulae for Impedances	33
3.4 Impedance Boundary Conditions	35
3.5 Transmission Line Concepts	36
4 Electron Cloud	39
4.1 Introduction	39
4.1.1 Single-bunch regime	40
4.1.2 Multi-bunch regime	42
4.2 The Electron Cloud build-up mechanism	43
4.2.1 Primary electron production	48
4.2.2 Secondary electron emission	49
4.2.3 Saturation effects	51
4.3 Electron Cloud effects	53
4.4 Conditioning and Mitigation	54
4.5 EC simulation code: PyECLOUD	56
5 Open Cell Metal Foams for Particle Accelerators	59
5.1 Open Cell Metal Foams	60
5.1.1 Electrical properties of conducting foams	63

5.1.2 Superconducting foams	68
5.2 Metal Foam vs Perforated metal patched pipes	68
5.2.1 Vacuum issues	68
5.2.2 Beam coupling impedance and parasitic losses	73
5.2.3 Secondary emission yield	78
6 Open Cell Metal Foams: Measurement and Numerical results	79
6.1 General Description of MU-EPSLNTM	79
6.2 Measurement Theory	81
6.3 Software and Measurement procedure	84
6.3.1 Calibration	86
6.3.2 Data Reduction	89
6.4 Measurement's Results	92
7 Conclusions.....	104
Appendix A-Maxwell's Equations	106
Appendix B- The Hamiltonian Formalism	108
Abbreviations	111
Acknowledgements	112
Bibliography	114

CHAPTER 1

Basic Concepts of the Accelerators

Accelerators are devices that control and manipulate the motion of charged subatomic particles (protons, electrons, neutrons) impressing high kinetic energies by the action of electromagnetic or electrostatic fields. The accelerated particles are sent against an appropriate “target” to investigate further the structure of matter and its constituents. Atoms are not elementary particles but composite entities with a complex internal structure. The basic idea is simple. Particles are grouped into two classes. The first contains heavy particles, called hadrons, such as neutrons and protons. The other one contains leptons, such as electrons and other light particles which interact weakly. In most experiments there are collisions of hadrons to high energy. This type of investigation was initially conducted using “natural” fast particles, as well as those emitted by radioactive substances or those making up the cosmic radiation. Subsequently, the construction of accelerators brought enormous advantages with respect to “natural” source both for the beam intensity and for the production of a multitude of new short-lived particles. The principle of phase stability is much important for the efficient working of accelerators and for the acceleration of particles to relativistic velocities. According to the principle one has stability when the particles are in the acceleration gap in synchronism with the accelerating electric field.[1] Depending on the acceleration device and the particle trajectory one has several type of accelerators:

- Electrostatic accelerators (Cockcroft and Walton Accelerator, Van de Graaff Accelerator, Tandem Accelerator)
- Linear accelerators (Linear Accelerator of Electrons, Linear Accelerator of Protons)
- Circular accelerators (Cyclotrons, Synchro-cyclotrons, Betatrons, Synchrotrons)

1.1 Structure and uses of accelerators

Characteristic elements of an accelerator are:

- the source of charged particles;
- the accelerating cavity surrounding the vacuum chamber in which the particles are released and accelerated;
- the generator of electric field;
- the focusing and the bending devices to maintain and concentrate the particles in a homogeneous beam of well-defined energy and trajectory;
- the nuclear target, inside or outside the acceleration chamber, subjected to the bombardment of the accelerated particles;
- various devices of measurement and control.[1]

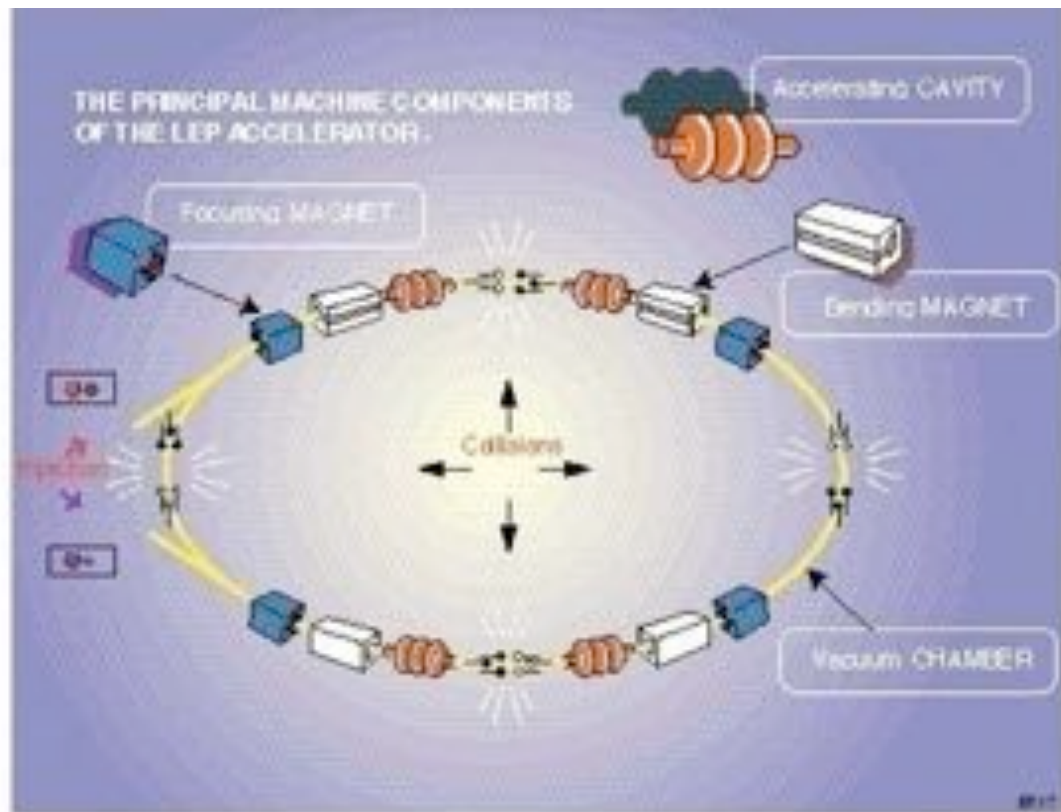


Figure 1.1: The principal machine components of the LEP Accelerators.

Use of accelerators has expanded beyond the traditional field of research in particle physics, with the development of specialized accelerators used for: [2]

- nuclear physics research including a broad spectrum of studies emphasizing energy precision, beam intensity, beam species and polarized beams;
- synchrotron radiation sources for a wide variety of applications of ultraviolet and x-ray beams in material science;
- medical applications in the therapy of tumors with penetrating X-rays;
- nuclear chemistry research through the polymerization by irradiation with electrons and X-rays, production of radioactive elements and radioactive isotopic tracers;
- radiobiology applications through the study of radiation effects on organic cells;

- industrial techniques such as the radiography of metals, study of their properties and the sterilization of food packaging.

1.2 Luminosity of a High Energy Collider

Because of the use of time varying fields to produce acceleration in high energy accelerators, these devices tend not to produce continuous particle beams, but rather beams that consist of a sequence of “bunches” of particles.

In colliding beam physics, two such beams are brought into collision.

Suppose one bunch of particles moving in one direction collides head on with a bunch moving in the opposite direction. Let the bunches both have cross-sectional area A and both contain N particles. Any particle in one bunch will “see” a fraction of the area of the other bunch $N\sigma_{int}/A$ obscured by the interaction cross section σ_{int} (the total area of overlap of two colliding particles). This situation is suggested in Figure 1.2. For our purposes we allow the entire interaction cross section to be attributed to the particles in one beam encountering a point test particle in the other beam.

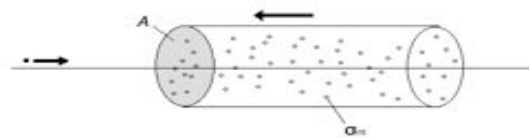


Figure 1.2: Collision of a single test particle from one beam with a particle bunch of the other beam.

The number of interactions per passage of two such bunches is then $N^2\sigma_{int}/A$. If the frequency of bunch collisions is f , then the interaction rate is

$$R = f \frac{N^2}{A} \sigma_{int}. \quad (1.1)$$

The luminosity, \mathcal{L} , is defined as the interaction rate per unit cross section:

$$\mathcal{L} = f \frac{N^2}{A} \quad (1.2)$$

That is, the luminosity contains all the factors in the above expression that we think we can control and hence represents a figure of merit for a collider. It would be surprising if beams came with bunches that were neat cylindrical uniformly populated volumes. Let us repeat the argument with a more realistic situation. Suppose that the particle distribution in the plane at right angles to the direction of motion is a “round Gaussian”, or more properly, a Rayleigh distribution. As a function of radius, r , in the cylindrically symmetric distribution, the density function for the distribution is

$$n(r) = \frac{N}{\sigma^2} e^{-\frac{r^2}{2\sigma^2}} \quad (1.3)$$

The contribution to the luminosity from two cylindrical shells at the same radius r and of the same thickness dr is

$$d\mathcal{L} = f \cdot \frac{dn}{2\pi r dr} \cdot dn \quad (1.4)$$

Then, after adding up the contribution to the luminosity from shells of different radius, we have

$$\mathcal{L} = f \frac{N^2}{4\pi\sigma^2}. \quad (1.5)$$

Luminosities are often expressed in $cm^{-2}s^{-1}$, for instance, LHC operates at a luminosity of $10^{34}cm^{-2}s^{-1}$. [2]

1.3 Linear beam dynamics

A detailed introduction to accelerator physics can be found in References [2–4], whence the treatment in this work is based. The motion of a particle of charge q in an accelerator is determined by the relativistic extensions to Newton's laws and the Lorentz force,

$$\frac{d\vec{p}}{dt} = q(\vec{E} + \vec{v} \times \vec{B}) \quad (1.6)$$

where \vec{v} is the particle velocity, \vec{E} is the electric field (used mainly for particle acceleration and longitudinal confinement), and \vec{B} is the magnetic field (used mainly to steer and focus

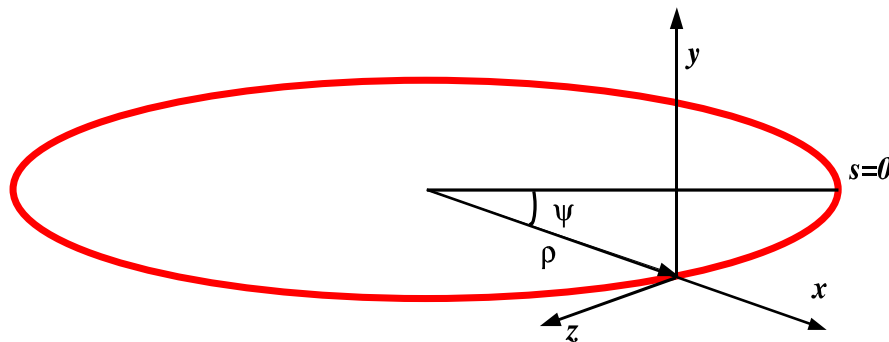


Figure 1.3 : Frenet-Serret coordinate system along the *design* orbit.

the particle motion). The relativistic particle momentum, \vec{p} is expressed as

$$\vec{p} = \gamma m \vec{\beta} c \quad (1.7)$$

where m is the rest mass, c is the speed of light, and $\vec{\beta}$ and γ are the relativistic velocity and beam Lorentz factor, respectively, defined as

$$\vec{\beta} = \vec{v}/c \quad (1.8)$$

$$\gamma = \frac{1}{\sqrt{1-\beta^2}} \quad (1.9)$$

To describe the particle's motion, it is useful to define a reference system as shown in Fig. 1.3 based on the *design* orbit in an ideal circular accelerator of radius ρ . The position of a particle may be parameterized in terms of an angle ψ , so that the arc length to a different point would be then $\Delta s = \rho \Delta \psi$. The local cartesian coordinate system described in Fig. 1.3 moving along with the beam particle is convenient for parameterization of the motion of a particle traveling on some trajectory slightly different from the design orbit. In this local system, the z -axis points in the direction of motion, the y -axis points up, and the x -axis points radially outward from the center of the circle. The local radius of the design orbit is determined by the vertical dipole field, B and the particle momentum according to

$$\rho = \frac{p}{qB} \quad (1.10)$$

where q is the particle charge. This relation is used to define the *magnetic rigidity* as $B\rho = p/q$, or the ratio of momentum to charge. It is written as a single symbol, $(B\rho)$, and for a particle with charge $q = Z|e|$ and atomic mass A , it is

conventionally calculated using the relation

$$B\rho [\text{T m}] = 3.33 p [\text{GeV}/c]A/Z \quad (1.11)$$

in units of [T m] when p is expressed in [GeV/c].

1.3.1 Magnetic fields and transverse particle motion

The magnetic fields in an accelerator can be expanded in terms of field multipoles. To first order, these fields are:

$$B_x = \frac{\partial B_y}{\partial x} y = -B_1 y, \quad (1.12)$$

$$B_y = -B_0 + \frac{\partial B_y}{\partial x} x = -B_0 + B_1 x, \quad (1.13)$$

where B_0 and B_1 are the dipole and quadrupole coefficients of the field. With these fields (assuming no longitudinal or horizontal magnetic fields are present), the transverse equations of motion for a reference particle along the accelerator circumference become

$$x'' + K_x(s) x = 0$$

$$y'' + K_y(s) y = 0$$

with

$$K_x(s) = \frac{1}{\rho(s)^2} - \frac{B_1(s)}{B\rho}$$

$$K_y(s) = \frac{B_1(s)}{B\rho} \quad (1.14)$$

where $x' = dx/ds$ (see Fig.1.3). The focusing functions $K_{x,y}(s)$ stress the analogy with a simple harmonic oscillator, in which the “spring constant” K is now a function of the position s . The general equation of motion is then expressed as

$$u'' + K_u(s)u = 0 \quad (1.15)$$

where u stands for either x or y in Eqs. 1.14. The function K_u is at least periodic in the accelerator circumference, L . Equation 1.15 is known as the *Hill's equation*, extensively studied during the 19th century. A solution of this equation reads

$$u(s) = A_u \sqrt{\beta_u(s)} \sin(\psi_u(s) + \psi_0) \quad (1.16)$$

where A_u is just a constant depending on the initial conditions, and $\psi(s)$ is the phase advance. The function $\beta_u(s)$ modulates the oscillation's amplitude and it is called *beta function*, β function, or the envelope function. It should not be confused with the relativistic speed $\beta = v/c$ in Eq. 1.8-1.9.

Inserting Eq. 1.16 into Hill's equation (Eq. 1.15) leads to the definition of another important parameter in accelerator physics, the betatron tune, Q defined as the number of oscillations per revolution around the accelerator;

$$Q_u = \frac{\psi_u(L)}{2\pi} = \frac{1}{2\pi} \int_{s_0}^{s_0+L} \frac{ds}{\beta_u(s)} \quad (1.17)$$

Equation 1.17 suggests that the β function can be interpreted as the local

wavelength of the oscillation. Depending on the literature, the tune of the accelerator is denoted by ν or Q . Other important parameters related to the β function are:

$$\alpha(s) = -\frac{\beta'(s)}{2} \quad (1.18)$$

$$\gamma(s) = \frac{1+\alpha(s)^2}{\beta(s)} \quad (1.19)$$

which are collectively known as the Courant-Snyder, or Twiss parameters. Again, note that $\gamma(s)$ is not the relativistic γ in Eq. 1.8-1.9. The importance of these parameters lies on the fact that at any location around the ring s , a trajectory in the phase space (u, u') has an area bounded by a curve

$$J = \gamma(s)u^2 + 2\alpha(s)uu' + \beta(s)u'^2 \quad (1.20)$$

where J is the single particle action, a constant of motion. It is also called the Courant-Snyder invariant. It is useful to characterize the beam by a particle that has an action that encloses a given fraction of the beam. For example, for a gaussian distributed beam this is the area in phase space containing the 34% of the beam particles. This is called the unnormalized rms emittance, ϵ_{rms} . A widely used convention is

$$\epsilon = 6\pi\epsilon_{\text{rms}} \quad (1.21)$$

known as the 95% emittance of the beam. That is, 95% of the beam particles in a gaussian beam have an action smaller than ϵ . The rms transverse beam size is given by[‡]

$$\sigma_t(s) = \sqrt{\epsilon_{\text{rms}}\beta(s)} \quad (1.22)$$

Note that the variables (u, u') are not canonically conjugate, as opposed to (u, p_u) (particle position and momentum). The relation between p_u and u' is

$$u' = \frac{p_u}{p} = \frac{p_u}{\gamma_r \beta_r m c} \quad (1.23)$$

where the subscript r has been introduced in γ_r and β_r to denote their relativistic meaning. The factor $\beta\gamma$ increases when the beam is accelerated, causing a decrease in u' and hence reducing ϵ . The *normalized* emittance,

$$\epsilon_n = \gamma_r \beta_r \epsilon \quad (1.24)$$

is invariant under acceleration, and eases the comparison of emittances at different energies. In terms of the normalized emittance, the rms beam size is given by

$$\sigma_t = \sqrt{\frac{\epsilon_n \beta}{6\pi \beta_r \gamma_r}} \quad (1.25)$$

1.3.2 Electric fields and longitudinal particle motion

So far only the influence of the magnetic field in Eq. 1.6 has been considered.

In the following, a brief review of the physics involved in the acceleration process and longitudinal capture/stability is presented by means of the electric

fields. The active accelerating elements are the *radio frequency* (rf) cavities, characterized by the frequency ω_{rf} of the longitudinal electric field oscillations and the peak voltage V . As for the transverse motion in Section 1.3.1, a more detailed description can be found in [2-4], on which the treatment in this section is based. Next and unless otherwise stated, the symbols β and γ used in the following refer to the relativistic velocity and Lorentz factor (Eq. 1.8-1.9), not to the Twiss parameters.

Motion of the synchronous particle

The fractional deviation of the particle's path length divided by the fractional deviation of the momentum is called the *momentum compaction* factor,

$$\alpha_p = \frac{dL/L}{dp/p} = \frac{p}{L} \frac{dL}{dp} \quad (1.26)$$

where L is the circumference of the design orbit.

The angular frequency of a particle circulating in a synchrotron is:

$$\omega = \frac{2\pi}{\tau} = \frac{2\pi\beta c}{L}, \quad (1.27)$$

where τ is the revolution period. Differentiation of Eq. 1.27 yields

$$\frac{d\tau}{\tau} = \frac{dL}{L} - \frac{d\beta}{\beta} = \left(\alpha_p - \frac{1}{\gamma^2} \right) \frac{dp}{p} \quad (1.28)$$

The expression within parentheses is usually written as

$$\eta \equiv \frac{1}{\gamma_t^2} - \frac{1}{\gamma^2} \quad (1.29)$$

and it is called the *slip factor*. Notice that at a particular energy $\gamma = 1/\sqrt{\alpha_p} = \gamma_t$, the slip factor η is zero. This is called the transition energy, whence the subscript t . Equation 1.29 yields a relation between the fraction revolution period deviation with the fractional momentum deviation given by

$$\frac{d\tau}{\tau} = \eta \frac{dp}{p} \quad (1.30)$$

Consider an rf cavity producing a wave of frequency ω_{rf} , and assume that it is an integer multiple of a particle's angular revolution frequency ω_0 , such that

$$\omega_{\text{rf}} = h\omega_0 \quad (1.31)$$

for some integer h , which is called the *harmonic number*. The subscript 0 in Eq. 1.31 has been added to denote the synchronous particle, that is, a particle that crosses the rf cavity gap on every turn when the rf phase is ψ_s and the voltage across the gap is $V \sin\psi_s$. The energy gained by the synchronous particle per revolution is

$$\Delta E_s = qV \sin\psi_s \quad (1.32)$$

However, not all the particles are synchronized with the rf field. So, it is useful to define the physical quantities of a particle relative to the synchronous one. Defining the relative phase difference $\phi = \psi - \psi_s$, and the difference in energy as $\Delta E = E - E_s$, the equations of motion for a particle with respect to the synchronous particle are:

$$\frac{d\phi}{dt} = \frac{\eta\omega_{rf}\tau}{\beta^2 E_s} \Delta E \quad (1.33)$$

$$\frac{d\Delta E}{dt} = eV(\sin\phi - \sin\phi_s) \quad (1.34)$$

For small phase oscillations, when $\sin\phi \approx \phi$, the two Eqs. 1.33-1.34 are merged in one,

$$\frac{d^2\phi}{dt^2} + (2\pi Q_s)^2 \phi = 0 \quad (1.35)$$

where Q_s is the *synchrotron tune*,

$$Q_s = \sqrt{-\frac{\eta\omega_{rf}\tau q V \cos\phi_s}{4\pi^2 \beta^2 E_s}} \quad (1.36)$$

Buckets and bunches

The phase oscillations described in Eq. (1.33-1.34) are represented in Fig. 1.4. The *unsynchronized* generic particle B (which arrives at the rf station with a phase difference ϕ , left) receives a kick larger than the synchronous particle. At the next rf station, the particle will arrive before the synchronous particle and it will receive a lower energy kick. This translates into a rotation around the synchronous particle on the longitudinal phase space plot (Figure 1.4, right). For a given set of rf parameters (voltage and harmonic number), unsynchronized particles within a certain area in phase space will undergo stable motion around the synchronous particle. The phase space trajectory of the particle that encloses the maximum area for stable motion is called the *separatrix* (Fig. 1.4, right), which defines the rf *bucket*. Because of this longitudinal stability, particles inside

the bucket rotate around the synchronous particle and constitute a *bunch*. These buckets exist as soon as the rf voltage is applied to the cavities. The number of buckets is given by $\omega_{rf}/\omega_s = h$, the harmonic number (Eq. 1.31). In principle, one can fill as many of these buckets with bunches as one wishes.

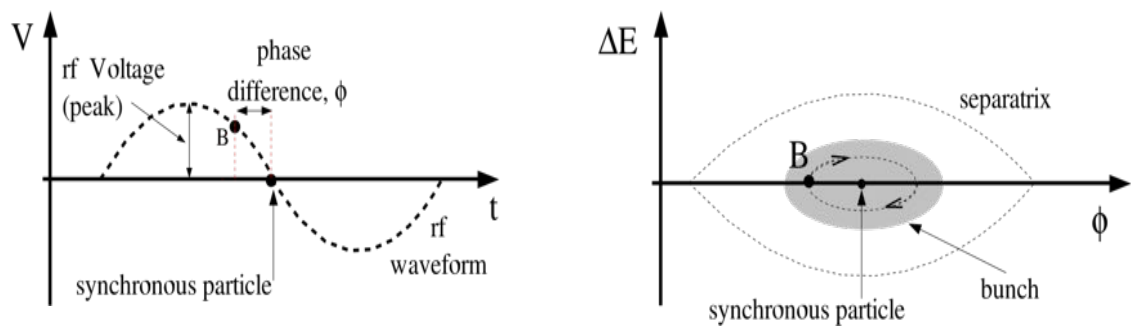


Figure 1.4: Bunch, bucket, separatrix. This is a non-accelerating bucket $\phi_s = 0$.

1.3.3 Phase stability of the bunched beam acceleration

We will find that there is a strong stability condition which dictates that particles near the ideal particle will indeed remain nearby, and oscillate about the ideal particle in energy, transit time space. These oscillations were first analysed for the device christened the synchrotron and so are called synchrotron oscillations. Of course, there are in reality three degrees of freedom for motion of the particle. We are going to describe the motion in the neighborhood of the ideal particle in all them eventually. Variations in energy and transit time are associated with one degree of freedom. Because transit time differences are equivalent to position differences along the general direction of motion of the ideal particle, this is called the longitudinal degree of freedom. It is not yet apparent that it is possible to treat this degree of freedom independently of the other two, the so called

transverse degrees of freedom. We will see that the frequency of longitudinal oscillation is generally much less than that of transverse oscillations and so, to a reasonable approximation, they are decoupled.

Let $V(t)=V_0\sin(h\omega_0t+\phi)$ be the gap voltage of the rf cavity, where V_0 is the amplitude, ϕ is an arbitrary phase angle, h is an integer called the harmonic number, $\omega_0=2\pi f_0$ is the angular revolution frequency, and f_0 is the revolution frequency of a synchronous particle. A synchronous particle is defined as an ideal particle that arrives at rf cavity at a constant phase angle $\phi = \phi_s$, where ϕ_s is the synchronous phase angle. The acceleration voltage at the rf gap and the acceleration rate for a synchronous particle are respectively given by

$$V_{rf} = V_0 \sin \phi_s, \quad \dot{E}_s = f_0 e V_0 \sin \phi_s, \quad (1.37)$$

Where e is the charge, E_s is the energy of the synchronous particle, and the overdot indicates the derivative with respect to time t .

A non-synchronous particle will arrive at the rf cavity at a phase angle ϕ with respect to the rf field, where ϕ can vary with time. At phase angle ϕ , the accelerating rate is $\dot{E} = f_0 e V_0 \sin \phi$, where f is the revolution frequency. The rate of change of the energy deviation is

$$\frac{d}{dt} \left(\frac{\Delta E}{\omega_0} \right) = \frac{1}{2\pi} e V_0 (\sin \phi - \sin \phi_s) \quad (1.38)$$

Where $\Delta E = E - E_s$ is the energy difference between the non-synchronous and the synchronous particles. Similarly, the equation of motion for the rf phase angle $\phi = -h\theta$, where θ is the actual angular position of the particle in a synchrotron, is

$$\frac{d}{dt} (\phi - \phi_s) = -h\Delta\omega = h\omega_0 \frac{\Delta T}{T} = h\eta\omega_0 \frac{\Delta p}{p} = \frac{\eta h \omega_0^2}{\beta^2 E} \frac{\Delta E}{\omega_0} \quad (1.39)$$

Equations (1.38) and (1.39) form the basic synchrotron equation of motion for

conjugate phase-space coordinates φ and $\Delta E / \omega_0$. This is the equation of motion for a biased physical pendulum system.[5]

CHAPTER 2

Synchrotron Radiation

Synchrotron radiation is the dominant factor in the design of high energy electron synchrotrons and is the obstacle to exceeding 100 GeV or so in this type of accelerators. In the proton case, single particle motion, to a very good approximation, exemplifies a Hamiltonian system. Particle motion in electron synchrotrons, on the other hand, is inherently dissipative. The energy loss due to synchrotron radiation and its replacement by the RF acceleration system leads to a variation with time of oscillation amplitudes in all three degrees of freedom, and we compute the related time constants. We will reproduce the Robinson's theorem, which relates these three time constants and demonstrates that there is a net damping effect that can be apportioned among the degrees of freedom at the choice of the designer. An electron storage ring will be designed to damp in each degree of freedom. The fact that the radiation process is quantized implies that there are statistical fluctuations in the radiation rate. These fluctuations cause excitation of synchrotron oscillations, and of betatron oscillations in at least one transverse degree of freedom.[2]

Accelerated charged particles, particularly electrons in a circular orbit, radiate electromagnetic energy. As far back in 1898, Lienard derived an expression for electromagnetic radiation in a circular orbit. Modern synchrotron radiation theory was formulated by many physicists; in particular, its foundation was laid by J. Schwinger.

Some of his many important results are summarized below:

- The angular distribution of synchrotron radiation is sharply peaked in the direction of the electron's velocity vector within an angular width of $1/\gamma$, where γ is the relativistic energy factor. The radiation is plane polarized on the plane of the electron's orbit, and elliptically polarized outside this plane.
- The radiation spans a continuous spectrum. The power spectrum produced by a high energy electron extends to a critical frequency $\omega_c = 3\gamma^3 \omega_\rho/2$, where $\omega_\rho = c/\rho$ is the cyclotron frequency for electron moving at the speed of light.
- Quantum mechanical correction becomes important only when the critical energy of the radiated photon, $h\omega_c = \frac{3}{2}hc\gamma^3/\rho$, is comparable to the electron beam energy, $E = \gamma mc^2$. This occurs when the electron energy reaches $mc^2(mc\rho/h)^{1/2} \approx 10^6 GeV$. The beamstrahlung parameter, defined as $|\Upsilon| = \frac{2}{3}h\omega_c/E$, is a measure of the importance of quantum mechanical effects.[5]

2.1 Radiation from relativistic particles

If a slowly moving particle of charge e undergoes an acceleration a , then the radiated power P is given by the Larmor formula:

$$P = \frac{1}{6\pi\epsilon_0} \frac{e^2 a^2}{c^3} \quad (2.1)$$

The angular distribution of the radiation varies as $\sin^2\theta$, where θ is the angle between the direction of the acceleration and the point of observation.

We can find the radiated power for relativistic charges by using the fact that radiated power is a Lorentz invariant. Suppose a photon of angular frequency ω' is traveling at a direction θ' with respect to the x' -axis in a “primed” frame that is moving parallel to the x -axis of the “unprimed” laboratory frame. Transformation to the unprimed frame gives

$$\tan \theta = \frac{\sin \theta'}{\gamma (\cos \theta' + \beta)} \quad (2.2)$$

$$\omega = \gamma \omega' (1 + \beta \cos \theta') \quad (2.3)$$

where γ is the Lorentz factor characterizing the relative motion of the two frames. If two photons are emitted at angles θ' and $\theta' + \pi$ with the same angular frequency ω' , then in the laboratory frame the total energy will be proportional to

$$\omega_1 + \omega_2 = 2\gamma\omega'. \quad (2.4)$$

If the emission takes place in a short interval τ' , then in terms of radiated power, the relation above can be written

$$P\tau = P' \tau' \gamma, \quad (2.5)$$

or $P=P'$, after recognition of the effect of time dilation. That is, the power that is lost to the Doppler shift in one direction is gained back in the other. So long as the angular distribution of radiation in the primed frame has the appropriate symmetry, we can conclude that the power is an invariant.

Look two cases: acceleration perpendicular to and parallel to the direction of motion of a relativistic charge. The first corresponds to a particle undergoing deflection in a bending magnet. In an inertial frame traveling at the speed of a particle and tangent to the orbit at the time of arrival of the particle, at the instant the particle will be at rest and undergoing acceleration in the $-y'$ direction. In this frame the power radiated is given by the Larmor expression, with a' inserted for the acceleration. For acceleration transverse to the relative direction of motion of the two frames, $a' = \gamma^2 a$. In the primed frame, the power distribution has the proper front-back symmetry needed for the argument of the preceding paragraph to be valid, so the power is invariant. As a result, the power in the laboratory frame is

$$\begin{aligned} P &= \frac{1}{6\pi\epsilon_0} \frac{e^2 a^2}{c^3} \gamma^4 \\ &= \frac{1}{6\pi\epsilon_0} \frac{e^2 c}{\rho^2} \gamma^4 \\ &= \frac{1}{6\pi\epsilon_0} \frac{e^4}{m^4 c^5} B^2 E^2 \end{aligned} \quad (2.6)$$

In the second form, a has been replaced by the centripetal acceleration c^2/ρ of a relativistic electron. The third form will be useful when we discuss radiation damping; here, E is the total energy, $E = \gamma mc^2$, and B is the magnetic field producing the curvature of the particle path's.

In contrast, suppose that the acceleration is in the direction of motion of the

charge. In the primed frame, the angular distribution just rotates by $\pi/2$, so our invariance-of-power argument is still all right. But now $a' = \gamma^3 a$, and so the power radiated in the laboratory frame is

$$P = \frac{1}{6\pi\epsilon_0} \frac{e^2 a'^2}{c^3} \gamma^6 \quad (2.7)$$

At first glance, this result looks even more ominous than the one for transverse acceleration. But such is not the case, in fact acceleration in the direction of motion of a rapidly moving particle is not as easily produced as transverse acceleration. Equation 2.8 can be recast in the form

$$P = \frac{2}{3} \frac{r_0}{mc^3} \dot{p}^2, \quad (2.8)$$

where r_0 is the classical radius of the particle.

So we will be concerned only with radiation arising from transverse acceleration. The radiation loss per turn on the design orbit of a synchrotron will be

$$U_0 = \int_0^{2\pi R} \frac{P}{c} dz \quad (2.9)$$

$$= C_\gamma E^4 R \left\langle \frac{1}{\rho^2} \right\rangle \quad (2.10)$$

where

$$C_\gamma = \frac{4\pi}{3} \frac{r_0}{(mc^2)^3} = 8.85 \times 10^{-5} \text{ m/GeV}^3 \quad (2.11)$$

and the square of the curvature $1/\rho$ is averaged over the circumference $2\pi R$ of the ring. The numerical coefficient has been evaluated for the electron, using $r_0 = 2,818 \times 10^{-15} \text{ m}$.

The average power radiated is

$$\langle P \rangle = fU_0 \quad (2.12)$$

where f is the orbit frequency $c/2\pi R$.

2.2 Damping of oscillations

With the inclusion of synchrotron radiation, the transverse and longitudinal oscillations of a single particle no longer have invariant amplitudes, for the system is now dissipative. In this section we calculate the damping rates. Note that a characteristic time for synchrotron radiation effects is the time τ_0 in which an electron of energy E would radiate E , i.e., and the rates will be expressed in terms of τ_0

$$\tau_0 \equiv \frac{E}{\langle P \rangle} \quad (2.13)$$

Synchrotron radiation reduces the momentum of a particle in the direction of its motion, while the acceleration system restores momentum parallel to the central orbit. Consider the case in which there is no net acceleration, as in beam storage. On the average, the two momentum increments are equal in magnitude. If, in an element of path ds , the particle radiates energy du and receives the same energy increment from the acceleration system, then the momenta before and after, \vec{p}_1 and \vec{p}_2 , are related by:

$$\vec{p}_2 = \vec{p}_1 - \frac{du}{c} \frac{\vec{p}_1}{p_1} + \frac{du}{c} \hat{u}_s \quad (2.14)$$

In the terms of the transverse and longitudinal components,

$$p_{2y} = p_{1y} - \frac{du}{c} \frac{p_{1y}}{p_1} \tag{2.15}$$

$$p_{2s} = p_{1s} - \frac{du}{c} \frac{p_{1s}}{p_1} + \frac{du}{c} \tag{2.16}$$

division of the first by the second gives the relationship between $y' = p_y/p_s$ before and after traversing ds :

$$y'_2 = y'_1 \frac{1 - du/E}{1 - du/E + du/cp_s} = y'_1 \left(1 - \frac{du}{E} \right) \tag{2.17}$$

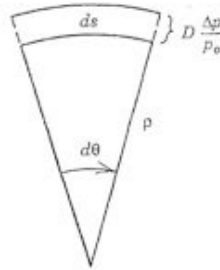


Figure 2.1: Illustration of increment in path length difference between off-momentum particle and ideal particle.

where E is the total energy of the particle, and we have kept only the lowest order term in du/E in the second equation. Therefore, the equation of motion in y contains a term

$$y'' = -\frac{1}{E} \frac{du}{ds} y' \tag{2.18}$$

in addition to the focusing term proportional to y . For a damping rate slow compared to the betatron oscillation frequency, the free oscillation then is just modified by the multiplicative factor

$$e^{-\frac{1}{2} \int \frac{1}{E} \frac{du}{ds} ds} = e^{-\frac{t}{2\tau_0}} \quad (2.19)$$

And so the damping time constant is

$$\tau_y = 2\tau_0 \quad (2.20)$$

Suppose the deviation from the synchrotrons energy of a particle is ΔE . In traversing an infinitesimal element of a turn, ΔE will change according to

$$\Delta E_2 = \Delta E_1 - du(\Delta E_1) + du(0) \quad (2.21)$$

where the second and third terms on the right are the energy loss due to synchrotron radiation at energy displaced from the synchronous energy ΔE_1 and the energy gain from the radiofrequency system at $\Delta E=0$ respectively. In terms of radiated power,

$$du(\Delta E_1) = P(\Delta E_1) dt_1 \quad (2.22)$$

$$du(\Delta E_1) = P(0) \left[1 + 2 \frac{\Delta E_1}{E} + 2 \frac{\Delta B}{B} \right] \left[1 + \frac{D}{\rho} \frac{\Delta E_1}{E} \right] dt_0 \quad (2.23)$$

$$du(0) = P(0) dt_0 \quad (2.24)$$

where dt_1 has been expressed in terms of the time element dt_0 on the synchronous orbit using Figure 1, and $P(\Delta E)$ has been written in terms of $P(0)$ using equation (2.5). The ΔB can be eliminated in favour of the fractional energy difference by the use of

$$\Delta B = B'x = B'D \frac{\Delta E}{E} \quad (2.25)$$

the change in ΔE per turn due to synchrotron radiation becomes

$$\frac{d\Delta E}{dn} = -\Delta E \int_0^T \frac{P(0)}{E} \left[2 + \frac{D}{\rho} + 2D \frac{B'}{B} \right] dt_0 \quad (2.26)$$

where T is the period of the synchronous orbit, the first term in the integral is just $2U_0/E$. Multiplying both sides by the orbit frequency, f , we obtain

$$\frac{d\Delta E}{dt} = -\Delta E \left[2 \frac{fU_0}{E} + \int_0^T \frac{fP(0)}{E} dt_0 D \left(\frac{1}{\rho} + 2 \frac{B'}{B} \right) \right] \quad (2.27)$$

The quantity fU_0/E is $1/\tau_0$, where τ_0 is the characteristic time for radiation processes. If we take τ_0 outside of the brackets, then, after cancellation of various coefficients, the result is:

$$\frac{d\Delta E}{dt} = -\frac{\Delta E}{\tau_0} (2 + \mathfrak{D}) \quad (2.28)$$

$$\mathfrak{D} = \frac{\langle \frac{D}{\rho^2} \left(\frac{1}{\rho} + \frac{B'}{B} \right) \rangle}{\langle \frac{1}{\rho^2} \rangle} \quad (2.29)$$

When this term is added to the equation of motion for a synchrotron oscillation, the solution for the motion will contain the factor

$$e^{-\frac{1}{2\tau_0}(2+\mathfrak{D})} \quad (2.30)$$

and so the time constant for damping in this degree of freedom is

$$\tau_s = \frac{2\tau_0}{2 + \mathfrak{D}} \quad (2.31)$$

Robinsons' theorem deduces the sum of the dumping rates for all three degrees of freedom. Since we already know the results for two of the modes, the theorem gives us the third immediately. The derivation goes as followed. Consider the transfer matrix of the six vector $x, x', y, y', \Phi, \Delta E$ through a path element ds . The diagonal elements for x' and y' will differ from unity by quantity $-du/E$, as we have seen above. The diagonal element for ΔE will differ from unity by the quantity $-2du/E$. The only terms in the determinant of the matrix that are first order in ds come from the diagonal elements. So for this infinitesimal matrix:

$$\det(dM) = 1 - 4\frac{du}{E} \quad (2.32)$$

the lowest order from one revolution

$$\det(M) = 1 - 4\frac{U_0}{E} \quad (2.33)$$

But the determinat is also the product of the eigenvalues. For oscillatory modes, the eigenvalues can be expressed as e^{γ_k} . The six γ_k occur in conjugate pairs, so the imaginary parts do not contribute to the product. If we call the real parts $\alpha_x, \alpha_y, \alpha_s$, then

$$\alpha_x + \alpha_y + \alpha_s = -2\frac{U_0}{E} \quad (2.34)$$

The α 's are the decrements per turn; multiplication by the orbit frequency gives the result for the time constants[2]:

$$\frac{2}{\tau_0} = \frac{1}{\tau_x} + \frac{1}{\tau_y} + \frac{1}{\tau_s} \quad (2.35)$$

$$\tau_x = \frac{2}{1-\mathfrak{D}} \tau_0. \quad (2.36)$$

CHAPTER 3

Wake Fields and Impedances

The wake fields we are most interested in is that seen by a test charge that follows the beam at a fixed relative distance. In the relativistic limit, causality dictates that there will be no electromagnetic field in front of the beam; thus the term “wake”. The rigid beam picture adopted in this chapter is not self-consistent, but is an excellent approximation for relativistic beams as far as the calculation of the wake fields is concerned. If the vacuum chamber is not a smooth pipe or if it is smooth but not perfectly conducting, a beam will generate behind it an electromagnetic wake (Figure 3.1).

3.1 Debye Potentials

In this section we briefly summarize the Debye potential formalism which provides a convenient reformulation of the Maxwell equations (see Appendix A) for computing the fields produced by particle beams in piecewise longitudinally invariant pipes.

We expect the fields produced by a transverse sheet of charge traveling in the (positive) z -direction with constant velocity v_0 :

$$\vec{j} = v_0 \rho_s(x, y) \delta(z - v_0 t) \vec{u}_z, \quad (3.19)$$

to share the same dependence on $z - v_0 t$. We thus switch to the spectral representation

$$\vec{f}(x, y, z, t) = \frac{1}{2\pi} \int_{-\infty}^{\infty} \vec{F}(x, y, k) e^{[-jk(z-v_0t)]} dk \quad (3.20)$$

where \vec{f} is any of the field vectors.

The spectral transverse fields in each homogeneous region can be computed from two (k -domain) Debye potentials Φ and Ψ [12], decomposing them into their irrotational and solenoidal parts (*Helmholtz-Clebsch* theorem).

$$\begin{cases} E_z = jk [1 - v_0^2 \tilde{\epsilon}(kv_0) \tilde{\mu}(kv_0)] \Phi + C/jk \\ H_z = jk [1 - v_0^2 \tilde{\epsilon}(kv_0) \tilde{\mu}(kv_0)] \Psi + C'/jk \end{cases} \quad (3.1)$$

Once the Debye potential have been computed, the complete solution of the EM problem is available: Eq. (3.1) gives the longitudinal components E_z, H_z , Eq. (3.2) furnish the irrotational parts of E_t, H_t , and finally Eqs. (3.3-3.4) yield the solenoidal parts of E_t, H_t :

$$\vec{E}_t^{(irr.)} = -\nabla_t \Phi, \quad \vec{H}_t^{(irr.)} = -\nabla_t \Psi \quad (3.2)$$

$$\vec{E}_t^{(sol.)} = -v_0 \tilde{\mu}(kv_0) \vec{u}_z \times \vec{H}_t^{(irr.)}, \quad (3.3)$$

$$\vec{H}_t^{(sol.)} = v_0 \tilde{\epsilon}(kv_0) \vec{u}_z \times \vec{E}_t^{(irr.)}, \quad (3.4)$$

Where $\tilde{\epsilon}(kv_0), \tilde{\mu}(kv_0)$ are the frequency dependent permittivity and permeability of the medium at $\omega = v_0$.

The longitudinal field components are, in turn:

$$E_z = jk \tilde{\gamma}^{-2}(kv_0)\Phi - C/jk, \tag{3.5}$$

$$H_z = jk\tilde{\gamma}^{-2}(kv_0)\Psi - C'/jk, \tag{3.6}$$

Where $\tilde{\gamma}(kv_0) = [1 - v_0^2\tilde{\epsilon}(kv_0)\tilde{\mu}(kv_0)]^{-1/2}$. The Debye potentials are computed by solving:

$$\nabla_t^2\Phi - k^2\tilde{\gamma}^{-2}(kv_0)\Phi = -\frac{\rho_s}{\tilde{\epsilon}(kv_0)} + C, \tag{3.7}$$

$$\nabla_t^2\Psi - k^2\tilde{\gamma}^{-2}(kv_0)\Psi = C', \tag{3.8}$$

Under suitable boundary conditions at the interface(s) between different media, which are readily obtained from the usual fields continuity conditions.

3.2 Coupling Impedances and Parasitic Loss

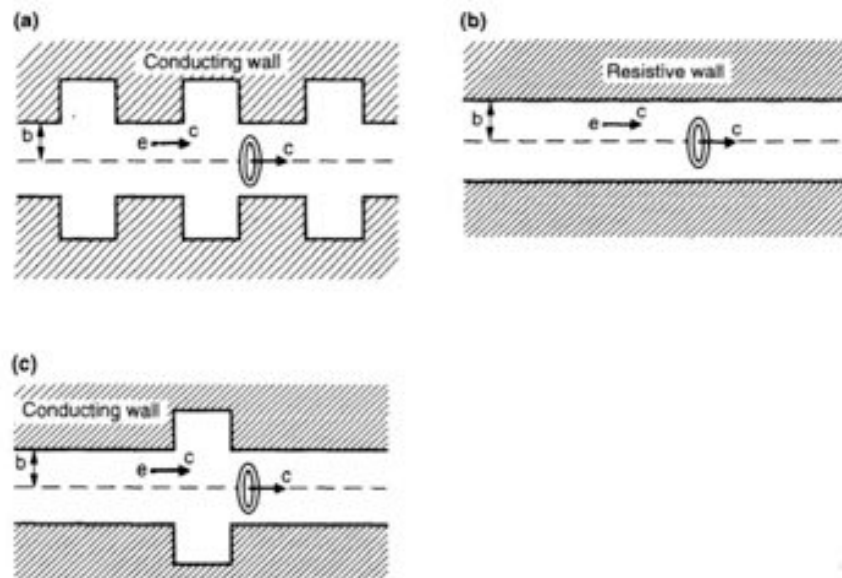


Figure 3.1: Examples of vacuum chamber pipe yhat generates wake fields. The beam is represented her as a ring passing a multipole moment with $\cos m\theta$ distribution. A test charge e following the beam at a fixed distance is shown. (a) Periodic structure. (b) Resistive wall. (c)

Single structure. In Figure 3.1(a), the force seen by the test charge varies periodically with the period of the structure. In Figure 3.1(c), the force occurs more or less as an impulse when the test charge passes by the wall structure.

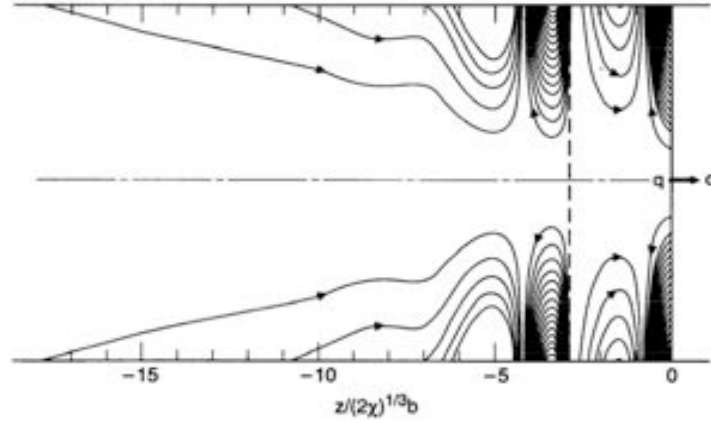


Figure 3.2: Wake electric field lines in a resistive wall pipe generated by a point charge q .

In a pipe with longitudinally-invariant cross section the force produced by a point of charge Q running parallel to the pipe axis, with (constant) velocity $\beta_0 c$ and transverse coordinate \vec{r}_0 , on another point of charge q travelling on a parallel trajectory, with transverse coordinate \vec{r}_1 at an (axial) distance s behind, is a function of \vec{r}_0 , \vec{r}_1 and s only, and can be derived from a scalar potential, w , called the wake potential per unit length:

$$\vec{F}(\vec{r}_0, \vec{r}_1, -s) = -qQ\nabla w(\vec{r}_1, \vec{r}_0, -s). \quad (3.9)$$

Where $\nabla = \{\nabla_{\vec{r}_1}, \partial_z, \vec{u}_z\}$. The principal parts of the longitudinal and transverse wake force in the limit as $\vec{r}_0, \vec{r}_1 \rightarrow 0$ are:

$$F_s = -qQ\partial_s w(0,0, s), \quad (3.10)$$

$$\vec{F}_\perp = -qQ\nabla_{\vec{r}_1} \nabla_{\vec{r}_0} w(\vec{r}_1, \vec{r}_0, s)|_{\vec{r}_0=\vec{r}_1=0} \cdot \vec{r}_0 = -qQ\partial_s \bar{w}(s) \cdot \vec{r}_0, \quad (3.11)$$

where $\bar{w}(s)$ is the transverse dyadic wake potential per unit length, obeying the *Panofsky-Wentzel* theorem:

$$\partial_s \bar{w}(s) = \nabla_{\vec{r}_1} \nabla_{\vec{r}_0} w(\vec{r}_1, \vec{r}_0, s) |_{\vec{r}_0 = \vec{r}_1 = 0} \quad (3.12)$$

The spectral coupling impedances per unit length are defined as follows [15],[1]:

$$Z_{\parallel} = \frac{1}{\beta_0 c} \mathcal{F}_{s \rightarrow k} \left(\frac{F_s}{qQ} \right), \quad \vec{Z}_{\perp} = \frac{j}{\beta_0 c} \mathcal{F}_{s \rightarrow k} \left(\frac{F_{\perp}}{qQ} \right), \quad (3.13)$$

where $\mathcal{F}_{s \rightarrow}$ denotes the $s \rightarrow k$ Fourier transform operator, with $k = \omega/\beta_0 c$. Note that the transverse impedance is a vector. Both have dimensions $ohm m^{-1}$.

The wake potential per unit length w can be computed from the electric Debye potential ϕ produced by the leading charge Q as follows [13]:

$$w(\vec{r}_1, \vec{r}_0, s) = \frac{(1 - \beta_0^2)}{Q} \phi(\vec{r}_1, \vec{r}_0, -s) \quad (3.14)$$

whence, using Eqs.(3.9-3.13) we get:

$$Z_{\parallel}(w) = jk \frac{(1 - \beta_0^2)}{\beta_0 c Q} \Phi(0, 0, k), \quad (3.15)$$

and:

$$\vec{Z}_{\perp}(w) = \vec{Z}_{\perp}(w) \cdot \vec{r}_0 \quad (3.16)$$

where:

$$\vec{Z}_{\perp}(w) = j \frac{(1 - \beta_0^2)}{\beta_0 c Q} \nabla_{\vec{r}_1} \nabla_{\vec{r}_0} \Phi(\vec{r}_1, \vec{r}_0, k) |_{\vec{r}_0 = \vec{r}_1 = 0} \quad (3.17)$$

is a tensor. Note that Z_{\parallel} and Z_{\perp} have dimensions $ohm m^{-1}$, while \vec{Z}_{\perp} has dimensions $ohm m^{-2}$.

From the longitudinal coupling impedance we can compute the parasitic loss, i.e. the energy lost by the beam per unit length, due to the finite conductivity of the chamber wall [1]:

$$\frac{\Delta \mathcal{E}}{L} = \frac{1}{2\pi} \int_{-\infty}^{+\infty} |I(w)|^2 \operatorname{Re}\{Z_{\parallel}(w)\} d\omega. \quad (3.18)$$

3.3 Perturbative Formulae for Impedances

From the Deybe potentials, the longitudinal and transverse coupling impedances can be computed as follows (see section 3.1):

$$Z_{\parallel}(w) = jk \frac{(1 - \beta_0^2)}{\beta_0 c Q} \Phi(\vec{r}_1, \vec{r}_0, k) \Big|_{\vec{r}_0 = \vec{r}_1 = 0}. \quad (3.22)$$

$$\bar{Z}_{\perp}(w) = j \frac{(1 - \beta_0^2)}{\beta_0 c Q} \nabla_{\vec{r}_1} \nabla_{\vec{r}_0} \Phi(\vec{r}_1, \vec{r}_0, k) \Big|_{\vec{r}_0 = \vec{r}_1 = 0} \quad (3.23)$$

where \vec{r}_0, \vec{r}_1 are the transverse positions of the leading and trailing particle, respectively.

Expressing the l.h.s in terms of fields instead of potentials, we have:

$$\begin{aligned} \Phi_0^* &= \frac{-E_{0z}^*}{jk(1 - \beta_0^2)}, \frac{\partial \Phi_0^*}{\partial n} \Big|_{\partial S_0} = \nabla_t \Phi_0^* \cdot \vec{u}_n = -E_{0n}^{*(irr.)}, \frac{\partial \Phi_0}{\partial n} \Big|_{\partial S} = \\ &= \nabla_t \Phi_0 \cdot \vec{u}_n = -E_n^{(irr.)}, \end{aligned} \quad (3.24)$$

$$\Phi \Big|_{\partial S} = \frac{E_z \Big|_{\partial S}}{jk(1 - \beta_0^2)} = \frac{Z_{wall} H_c \Big|_{\partial S}}{jk(1 - \beta_0^2)} = -\frac{Y_0 Z_{wall}}{jk(1 - \beta_0^2)} (\beta_0 E_n^{(irr.)} + \beta_0^{-1} E_n^{(sc)}) \quad (3.25)$$

In the Eq.(3.25) the fields E_{0n}, E_{0z} refer to the *unperturbed* situation, while E_n, E_z, H_c refer to the *perturbed* one. The second equality in 3.25 follows by assuming a Leontovich boundary condition [14] at the pipe wall (see section 3.4):

$$\vec{u}_n \times [\vec{u}_n \times \vec{E} - Z_{wall} \vec{H}]_{\partial S} = 0 \quad (3.26)$$

where, for a resistive wall with conductivity σ ,

$$Z_{wall} = Z_0 (1 - j\sigma/kv_0\epsilon_0)^{-1/2} \quad (3.27)$$

in the complex characteristic impedance of the wall material evaluated at $\omega = kv_0$.

So, we get [13]:

$$\begin{aligned} Z_{\parallel}(w) = & Z_{0\parallel}(w) \\ & + \frac{\epsilon_0}{\beta_0 c Q^2} \{ Y_0 \oint_{\partial S} Z_{wall} E_{on}^{(irr.)*}(\vec{r}, 0) [\beta_0 E_n^{(irr.)}(\vec{r}, 0) \\ & + \beta_0^{-1} E_n^{(sol.)}(\vec{r}, 0)] d\ell - \oint_{\partial S} E_{0z}^*(\vec{r}, 0) E_n^{(irr.)}(\vec{r}, 0) d\ell \} \end{aligned} \quad (3.28)$$

where we used the well known fact that the longitudinal impedance of a perfectly conducting pipe (*unperturbed* situation) is a pure reactance.

Furthermore, using the dyadic Panofsky-Wentzel theorem, by the first applying the dyadic differential operator $\nabla_{\vec{r}_0} \times \nabla_{\vec{r}_1}$ to both sides of the identity, then letting $\vec{r}_0, \vec{r}_1 \rightarrow 0$, and finally using Eq.(3.23), we get:

$$\begin{aligned} \bar{Z}_{\perp}(w) = & \bar{Z}_{0\perp}(w) + \frac{\epsilon_0}{\beta_0 c Q^2 k} \{ Y_0 \oint_{\partial S} Z_{wall} \nabla_{\vec{r}_0} E_{on}^{(irr.)*}(\vec{r}, \vec{r}_0) \times \nabla_{\vec{r}_1} [\beta_0 E_n^{(irr.)}(\vec{r}, \vec{r}_1) \\ & + \beta_0^{-1} E_n^{(sol.)}(\vec{r}, \vec{r}_1)] d\ell - \oint_{\partial S} \nabla_{\vec{r}_0} E_{0z}^*(\vec{r}, \vec{r}_0) \times \nabla_{\vec{r}_1} E_n^{(irr.)}(\vec{r}, \vec{r}_1) d\ell \} \Big|_{\vec{r}_0=\vec{r}_1=0} \end{aligned} \quad (3.29)$$

Equations (3.28-3.29) represent our general results relating the *perturbed* and *unperturbed* coupling impedances. They show the different role played by the boundary and material perturbations in a particularly neat fashion. As a matter of fact, the r.h.s of eqs. (3.28-3.29) is the sum of two terms: the first is nonzero if and only if Z_{wall} is not identically zero on ∂S , and accordingly accounts for the effect of the constitutive properties of the wall. The second integral, on the other hand, is non-zero if and only if the *unperturbed* axial field component E_{0z} is

not identically zero on ∂S , and thus accounts for the effect of the geometrical perturbation of the boundary. Accordingly the second integral in (3.28-3.29) effectively spans only the geometrically *perturbed* boundary subset $\partial S - \partial S_0$.

3.4 Impedance Boundary Conditions

Accelerator pipes are usually composed of several conducting shells with different electrical properties, possibly separated by non-conducting (e.g., vacuum) layers. In order to compute the electromagnetic field within such structures one has to solve, in principle, Maxwell equation in *each* homogeneous region, enforcing the usual boundary conditions (continuity of the tangential components of the electric and magnetic fields at the interfaces between material media with different electric/ magnetic properties). In many instances, on the other hand, one is only interested in computing the field in one region S only, e.g., the beam chamber. In this case, impedance boundary conditions, when applicable [14], can substantially improve computational efficiency.

In the simplest case, impedance boundary conditions read:

$$\hat{n} \times [\hat{n} \times \vec{E} - Z_{wall} \vec{H}]_S = 0, \quad (3.30)$$

Where S is the boundary of the problem's domain (wall), Z_{wall} describes the external medium beyond the wall, and \hat{n} the outward unit vector normal to S . These conditions are credited to *Y. Leontovich* [36]. The heuristic principle behind them is discussed below.

For a plane wave incident on an optically lossy half-space, the transmitted field wave-vector is normal to the interface plane S , for any angle of incidence. Thus in the lossy half-space including S^+ (the face of S inside the lossy medium) one has in the spectral domain:

$$\hat{n} \cdot \vec{E} = \hat{n} \cdot \vec{H} = 0, \quad \hat{n} \cdot \vec{E} = Z\vec{H}, \quad (3.31)$$

$$Z = Z_0 \left(1 - j \frac{\sigma}{\omega \epsilon_0}\right)^{-1/2},$$

Where Z is the characteristic impedance of the lossy material, $Z_0 = 376.7 \text{ ohm}$ the free space wave impedance, and \hat{n} unit vector normal to S pointing toward the lossy medium. The tangential field components being continuous across S , equation (3.30) holds true on S^- (the face of S outside the lossy medium) as well. The applicability of Leontóvich conditions to more general situations relies on the following heuristic arguments. The plane-wave incident field assumption can be relaxed, provided the medium is sufficiently throughout the whole plane wave spectrum of the incident field. The plane interface assumption, on the other hand, can be relaxed provided S can be viewed as *locally* plane within the first Fresnel zone drawn on the (plane) wavefront tangent to S^+ . The radius of the first Fresnel zone goes to zero with the wavelength inside the medium, i.e., as $|n|$ goes to infinity, n being the boundary material refraction index. A sufficient condition which fulfills all requirements above is [14]:

$$I_m(n) k R \gg 1 \quad (3.32)$$

Throughout the whole k -spectrum of the incident field, R being the (local) curvature radius of the boundary surface. A further condition is that the surface properties should be uniform on a scale of the order of the medium wavelength. Equation (3.27) is verified in a wide variety of practical relevant cases, and Leontóvich conditions are accordingly widely used in microwave engineering.

3.5 Transmission Line Concepts

Voltage and current waves in uniform transmission lines are described, (in the

time harmonic or frequency domain representations), by :

$$V(z) = V^+ e^{-j\beta z} + V^- e^{j\beta z}, \quad I(z) = Y_0 [V^+ e^{-j\beta z} - V^- e^{j\beta z}], \quad (3.33)$$

where V^+, V^- are the complex amplitudes of the forward and backward voltage waves, β, Y_0 are the medium propagation constant and characteristic admittance, respectively.

The (voltage) reflection coefficient:

$$\Gamma(z) := \frac{V^- e^{j\beta z}}{V^+ e^{-j\beta z}} = \Gamma(0) e^{2j\beta z} \quad (3.34)$$

Is the ratio between the complex amplitude of the reflected and incident voltage waves. Using eq. (3.34) in (3.33) we get:

$$V(z) = V^+ e^{-j\beta z} [1 + \Gamma(z)], \quad I(z) = Y_0 V^+ e^{-j\beta z} [1 - \Gamma(z)]. \quad (3.35)$$

The local impedance on a (uniform) transmission line is defined by:

$$Z := \frac{V(z)}{I(z)} = Z_0 \frac{1 + \Gamma(z)}{1 - \Gamma(z)}. \quad (3.36)$$

Equations (3.34) and (3.36) allow to obtain the input impedance of a homogeneous transmission line tract of length ℓ terminated into a load impedance Z_L . In fact, once $Z(0) = Z_L$ is known, so is $\Gamma(0)$ from (3.36). then eq.(3.34) gives $\Gamma(-\ell)$, and from this using again (3.36) one gets the input impedance $Z(-\ell)$. Iterating the above reasoning, one can easily compute the input impedance of several cascaded homogeneous transmission line extending to infinity, for which $V^- = 0$, is Z_0 at any z .

Consider now the two port network representing a line tract with propagation constant β and characteristic impedance $Z_0 = 1/Y_0$, where V_2, I_2 and V_1, I_1 are the voltage and current at the output ($z = 0$) and input ($z = -\ell$) ports, respectively. The transmission matrix relates the output quantities to the input

ones as follows:

$$\begin{cases} V_2 = \mathcal{A}V_1 + \mathcal{B}I_1 \\ I_2 = \mathcal{C}V_1 + \mathcal{D}I_1 \end{cases} \quad (3.37)$$

Specializing (3.33) at the output ports $z = 0, -\ell$ gives:

$$V_2 = V^+ + V^-, \quad I_2 = Y_0[V^+ - V^-], \quad (3.38)$$

$$V_1 = V^+ e^{j\beta\ell} + V^- e^{-j\beta\ell}, \quad I_1 = Y_0[V^+ e^{j\beta\ell} - V^- e^{-j\beta\ell}], \quad (3.39)$$

whence one easily obtains V^+ and V^- as function of V_1, I_1 . Substituting back in (3.37) and comparing with (3.39) one gets:

$$\mathcal{A} = \cos(\beta\ell), \quad \mathcal{C} = Y_0 \cos(\beta\ell), \quad \mathcal{B} = -jZ_0 \sin(\beta\ell), \quad \mathcal{D} = -j \sin(\beta\ell). \quad (3.40)$$

CHAPTER 4

Electron Cloud

The Electric fields present in a vacuum chamber accelerate electrons (produced by field emission, photo-emission, residual gas ionization, etc) towards the wall chamber surface. If the bombarding electrons acquire enough energy, they produce secondary electrons when they hit the chamber wall, which in turn are accelerated by the electric field normal to the surface. These electrons may bombard again another surface and emit secondary electrons. If the appropriate combination of surface properties and electric fields are fulfilled, this bouncing back and forth between surfaces develops an electron multiplication, or *multipacting effect*, which creates a cloud of electrons inside the vacuum chamber. The *electron cloud* in accelerators is defined as an accumulation of electrons inside the beam pipe which, if sufficiently strong, can affect the machine performance by increasing the vacuum pressure, producing emittance growth, causing beam loss, cryogenic heat load or interference of the beam diagnostics [8].

4.1 Introduction

In the field free regions of accelerators, the electric field producing the multipacting is provided by the beam, so that the two components influencing the electron accumulation are the beam and the chamber surface characteristics. Among this, the most relevant is the Secondary Electron Yield (SEY, or δ) of the chamber material and its dependence on the impinging electron energy. An

example of this dependence is shown in Fig. 4.1. For a given electron, more than one secondary electron are produced if the electron energy is larger than E_1 and smaller than E_2 . Motivated by the predicted detrimental consequences on the future LHC collider at CERN, the electron cloud has been studied using RF test benches in laboratory set-ups [9,10]. However, the conditions in an accelerator are different. Next, the electron cloud characterization depending on the accelerator beam parameters is shown. The electron cloud is mainly classified into two different regimes: single-bunch and multi-bunch regime. For the regions with electric or magnetic elements (such as RF cavities, bending magnets, et cetera), the field becomes a combination of beam and the external field for each case.

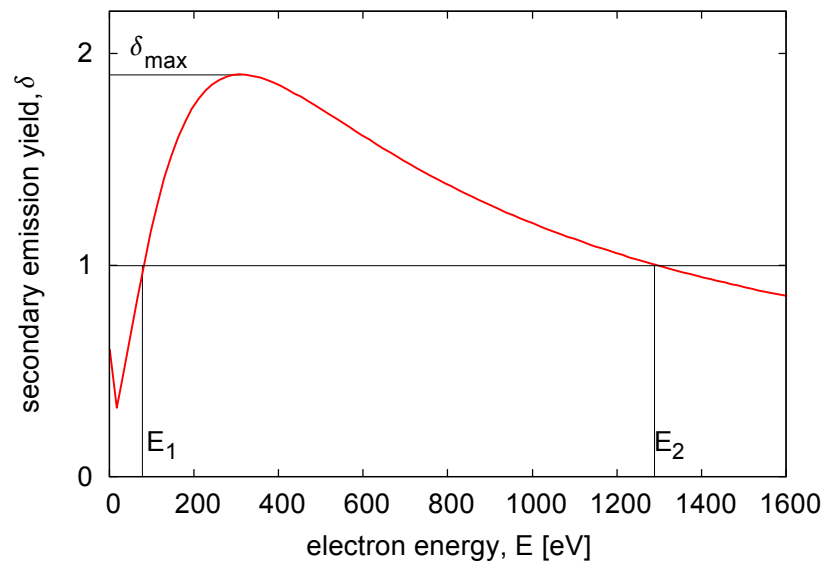


Figure 4.1: Typical behaviour of the secondary electron yield as a function of the impinging electron energy. The behaviour changes for different materials, with different δ_{\max} , E_1 , E_2 , etc.

4.1.1 Single-bunch regime

The single-bunch regime occurs if the length of the (positively charged) bunch is long enough to sustain multiple passes of electrons. It is also called *trailing edge* multipacting. Electrons are attracted by the beam potential, and their motion is characterized by the electron bounce frequency [11],

$$\omega_e = c\sqrt{2\pi r_e \lambda_p} \quad (4.1)$$

where r_e is the classical electron radius, and λ_p is the volume density of the beam. After the passage of the bunch density peak, electrons are released and accelerated by the part of the beam of decreasing density (trailing edge of the beam density distribution, see Fig.4.2). The number of electrons inside the chamber grows dramatically upon such trailing edge multipacting, as observed at the PSR and expected in the SNS ring [12]. The build-up is typically not sensitive to the bunch spacing, and it critically depends on the length of the bunch and the variations in its longitudinal density, which determine the energy gain and the multipacting duration. Upon acceleration by the beam, the electron energy is typically below the keV level. Associated with the electron cloud build up, pressure rises, and single-bunch, transverse instabilities are observed [13].

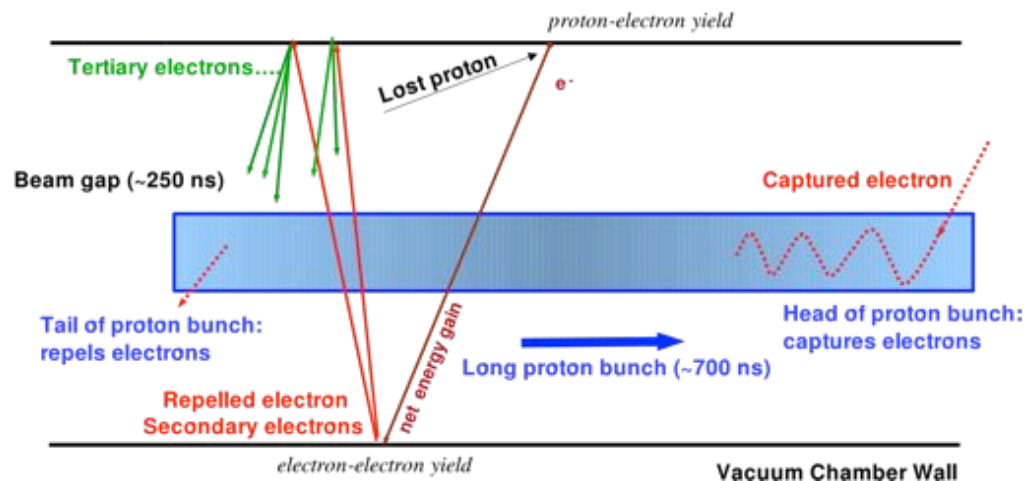


Figure 4.2: Single-bunch multipacting schema at the PSR. Courtesy of J. Wei [13].

4.1.2 Multi-bunch regime

In this case, the electron accumulation occurs under the passage of successive positively charged bunches [12,14]. The primary electrons can be created by photoelectrons (produced from synchrotron radiation), ionization of residual gas, and when stray particles hit the chamber walls. These primary electrons gain energy due to the interaction with the passing bunch, or under successive bunch passages. A multipacting effect can develop if two conditions are fulfilled:

- the energy gain is such that it can generate more than one secondary electron after impinging the chamber wall. In Fig. 4.1, this is at an energy larger than E_1 , and smaller than E_2 .
- the survival time of these secondary electrons is comparable to the bunch spacing.

This mechanism was first described as *beam-induced multipacting* (BIM) in Ref. [15]. For a round chamber of radius b , BIM was historically presented as almost a resonance: the time by which the electrons cross the vacuum pipe is in

synchronism with the bunch passages, which leads to [14,15]

$$N_b \leq \frac{b^2}{r_e s_b} \quad (4.2)$$

where N_b is the bunch population, and s_b is the bunch spacing (in units of length). However, Eq. 4.2 is far too stringent. Since most of the secondary electrons travel with very low energy, and in addition, the SEY for this low energy is close to unity, their survival time can be very long. Thus electron clouds occur even for bunch spacings much larger than that suggested by Eq. 4.2. Electron clouds are observed in machines with short bunch spacings, ($s_b/c \approx 4-8$ ns, like with the positron beams in KEK-B and PEP-II), and long bunch spacings

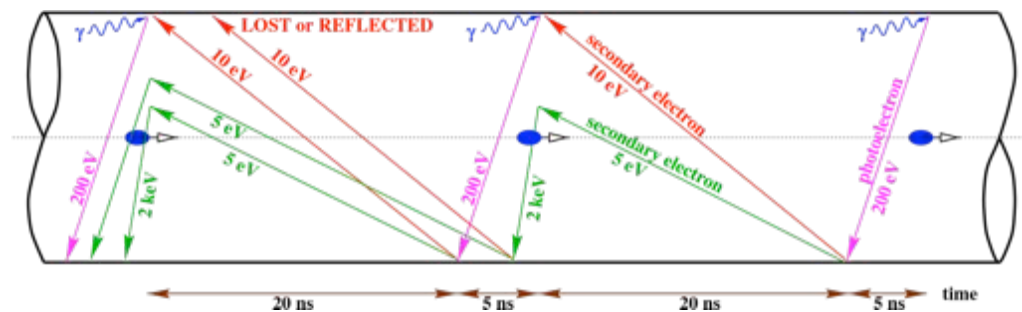


Figure 4.3: Multipacting schema in the LHC. Courtesy of F. Ruggiero.

($s_b/c \approx 25-200$ ns, like with the hadron beams in SPS or RHIC). An interesting result is that, due to the purely electromagnetic nature of the interaction driving the electron cloud mechanism, electron clouds have also been found with electron beams at the APS [16], albeit at a more modest level compared to the positron beams in the same machine.

4.2 The Electron Cloud build-up mechanism

If we want to find a simple analytical model to describe this process, considering an empty chamber before the injection and a train of uniformly spaced bunches, we can write [19]:

$$n_{i+1} = \delta_{\text{eff},i} n_i + n_0 \quad (4.3)$$

where n_{i+1} is the number of electrons in the chamber at the instant t_i , right before of the i -th bunch, n_0 the number of seeds generated after the first passage and $\delta_{\text{eff},i}$ n_i which defines the average of $\delta(E)$ over all electron-wall collision during the time window (such a quantity can also be negative, when the wall acts like a net electron absorber). The quantity $\delta_{\text{eff},i}$ can be directly related to the SEY of the chamber's surface $\delta(E)$ and to the energy spectrum of the impacting electrons, since we can write:

$$n_{i+1} = n_i + \int_0^\infty \int_{t_i}^{t_{i+1}} \Phi(E, t) (\delta(E) - 1) dt dE + n_0 \quad (4.4)$$

where:

$$\Phi(E, t) = \frac{dn}{dE} \quad (4.5)$$

is the instantaneous energy spectrum of the electrons impinging the wall. If we define the normalized energy spectrum for the the i -th bunch passage as:

$$\phi_i(E) = \frac{1}{n_i} \int_{t_i}^{t_{i+1}} \Phi(E, t) dt \quad (4.6)$$

we can rewrite the Eq. 4.4 as:

$$n_{i+1} = n_i \left(1 + \int_0^\infty \phi_i(E) (\delta(E) - 1) dE \right) + n_0 \quad (4.7)$$

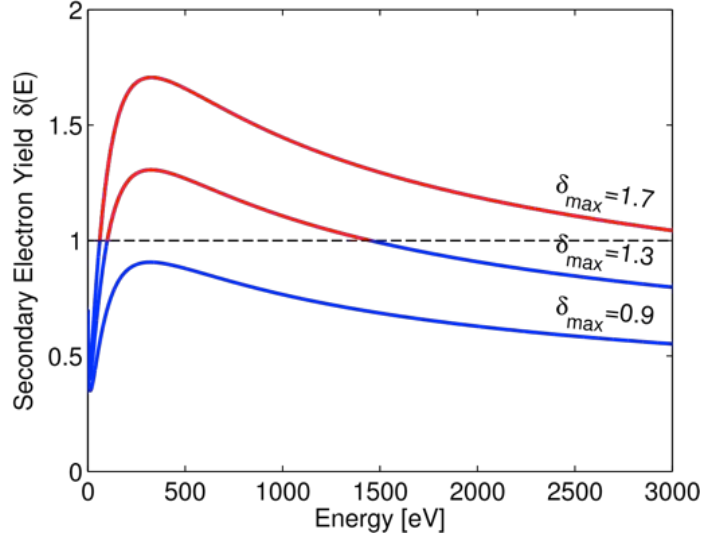


Figure 4.4: SEY curve for different values of the δ_{\max} parameter. The values for which the material behaves as electron absorber or emitter are plotted in blue and red respectively [11].

and, comparing against Eq. 4.3, we obtain:

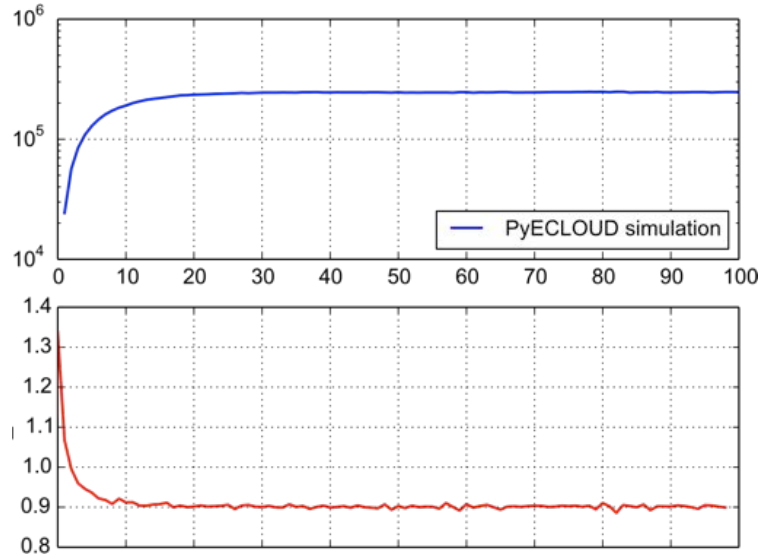
$$\delta_{\text{eff},i} = 1 + \int_0^\infty \phi_i(E) (\delta(E) - 1) dE \quad (4.8)$$

As shown in Fig. 4.4, for different values of δ_{\max} it is possible to recognize two regions of the SEY curve depicted in blue and red. The blue one is for $\delta(E) < 1$, which means that the walls act as an electron absorber; in the other case, for $\delta(E) > 1$, the walls act as an electron emitter.

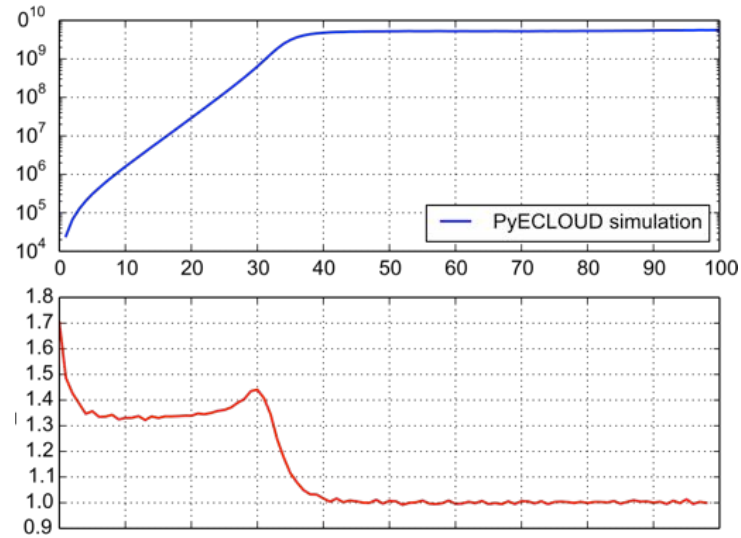
If we suppose that the electrons do not influence each other's trajectory, which means that the Coulomb forces between them are negligible, we can assume that $\delta_{\text{eff},i}$ does not depend on the bunch index:

$$\delta_{\text{eff},i} = \delta_{\text{eff}} \quad (4.9)$$

$$\Phi_i(E) = \phi(E) \quad (4.10)$$



(a) Simulated EC build up for $\delta_{\text{max}} = 1.10$. Top: number of electrons for each bunch passage.
Bottom: δ_{eff} computed by Eq. 4.9



(b) Simulated EC build up for $\delta_{\text{max}} = 1.80$. Top: number of electrons for each bunch passage.
Bottom: δ_{eff} computed by Eq. 1.7

Figure 4.5: Simulated EC build up for two possible value of δ_{max}

In these conditions by recursively applying Eq. 4.7 we find:

$$n_i = n_0 \sum_{k=1}^i \delta_{eff}^k \quad (4.11)$$

which is a partial sum of a geometric series and can be written as:

$$n_i = n_0 \frac{1 - \delta_{eff}^{i+1}}{1 - \delta_{eff}} \quad (4.12)$$

According to this, it is possible to define two different conditions (see Eq. 4.8):

- $\delta_{eff} < 1$: the EC grows linearly in time following beam injection into an empty chamber and, after, it tends to a constant value, which is essentially an equilibrium condition between primary electron production and electron absorption at the chamber's wall. This regime is called as "**seed accumulation regime**" [17, 19].
- $\delta_{eff} > 1$: the number of electrons in the chamber grows exponentially; this condition is called as "**multipacting regime**" because it indeeds an avalanche multiplication of electrons driven by secondary emission. This build up process stops when the EC space-charge is strong enough to repel the electrons against the walls of the chamber, at which point δ_{eff} becomes equal to 1 and a dynamical equilibrium is reached.

The value of δ_{max} for which $\delta_{eff} = 1$ is called "**multipacting threshold**" and separates the seed accumulation and the multipacting regimes. It can be easily recognized plotting the number of electrons in the beam chamber versus the SEY.

4.2.1 Primary electron production

According to the type of machine and the energy of the accelerated particles, the EC build-up is related to two different mechanism for the generation of primary electrons: the beam induced an ionization of the residual gas and the photoemission due to synchrotron radiation.

- **Residual gas ionization:** the particle of the beam can ionize the molecules of the residual gas in the beam chambers (where vacuum pressures are typically below 10^{-8} mbar) producing free electrons. The local electron production rate per unit volume in the beam chamber is given by:

$$\frac{dn_{ion}}{dt} = \sigma_{ion} n_{gas} \varphi_p \quad (4.13)$$

where σ_{ion} is the ionization cross section of the residual gas [20], n_{gas} is the residual gas density (supposed to be uniform in space and constant on the time scale of few beam revolutions), and φ_p is the beam particle flux (per unit area)[21]. For proton beams, the number of seeds produced by gas ionization is higher for beam energies below 2 TeV[22]. For this reason, the EC effects has been observed to occur also in the PS and the SPS where the energy goes up to 26 GeV for the PS and up to 450 GeV for the SPS.

- **Photoemission due to synchrotron radiation:** synchrotron radiation is the emission of photons that occurs when a particle beam undergoes a transverse acceleration [21, 22], for example in a bending magnet. The total power emitted by the beam due to the bending dipoles can be written as:

$$P = \frac{q\gamma_{real}^4}{3\epsilon_0} I_{beam} \quad (4.14)$$

where q is the particle charge, γ_{real} is the relativistic factor, I_{beam} is the

beam current.

The minimum photon energy needed to create a photoelectron depends on the beam chamber's material work function, that typically is of few eV. If the beam energy is large enough, the photons can extract electrons from the chamber's wall[23]. These electrons are typically called "photoelectrons" and can constitute the main source of primary electrons in the buildup of the EC, when the energy of the beam is large enough, for example in the LHC at collision energy. The synchrotron radiation is emitted in the direction tangent to the beam trajectory. The number of electrons produced per incident photon is defined as the "Photoelectron Yield" of the chamber surface, which depends on several parameters like the photon energy, the angle of incidence and the properties of the technical surface.

4.2.2 Secondary electron emission

The capability of a solid surface to emit secondary electrons, once it is irradiated by electrons, is called $\delta(E)$. It is a function of the primary electron energy, its angle of incidence and of the composition and history of the chamber surface. The SEY is defined as the ratio between the electron emitted current and the corresponding impinging onto wall current:

$$\delta(E) = \frac{I_{emit}(E)}{I_{imp}(E)} \quad (4.15)$$

Typically for materials employed for accelerators vacuum chamber, this function has a maximum value (δ_{max}) in a range of $1 \div 3$ at an energy of $200 \div 600$ eV.

A typical SEY curve is presented in Fig. 4.6, this quantity can in turn be

decomposed in two main components following the equation [11]:

$$\delta(E) = \delta_{\text{elas}}(E) + \delta_{\text{true}}(E) \quad (4.16)$$

where $\delta_{\text{elas}}(E)$ and $\delta_{\text{true}}(E)$ correspond respectively to electrons which are elastically reflected by the surface and to the so called “true secondaries”. The first component, corresponding to the green curve in Fig.4.6, can be parametrized as:

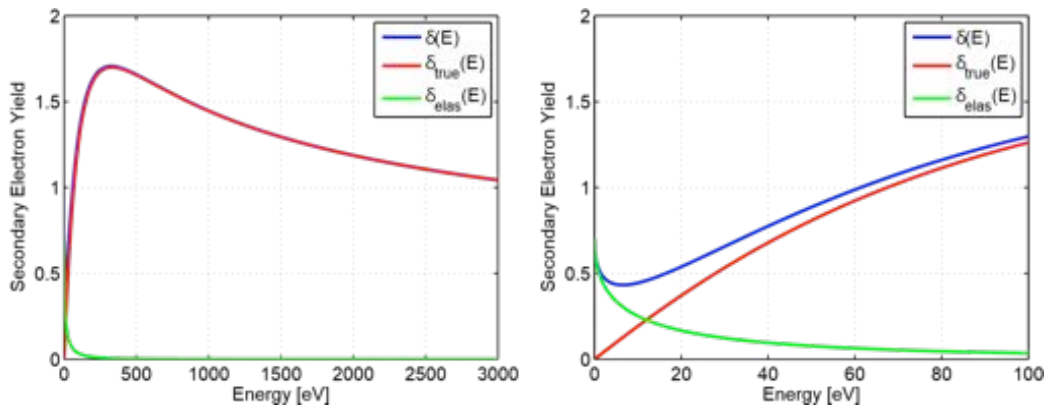


Figure 4.6: Left: SEY curve for $\delta_{\text{max}} = 1.7$ - elastic component $\delta_{\text{elas}}(E)$, “true secondary” component $\delta_{\text{true}}(E)$, and total $\delta(E)$. Right: zoom on the low energy region [11].

$$\delta_{\text{elas}}(E) = R_0 \left(\frac{\sqrt{E} - \sqrt{E + E_0}}{\sqrt{E} + \sqrt{E + E_0}} \right)^2 \quad (4.17)$$

where R_0 and E_0 are two free parameters of the model [24]. These electrons are generated by an elastic interaction with the surface of chamber and are emitted with the same energy with which they impacted on the surface. The “true secondary” component has the form:

$$\delta_{\text{true}}(E) = \delta_{\text{max}} \frac{s \frac{E}{E_{\text{max}}}}{s - 1 + \left(\frac{E}{E_{\text{max}}}\right)^s} \quad (4.18)$$

where s is a free parameter and E_{max} is the value of energy corresponding to the maximum SEY curve. These electrons are emitted from the surface of the chamber after the impact of the electrons, which have enough energy to win the work function of the material. It is quite intuitive to understand that the essential ingredient for the build-up of the EC is the SEY of the chamber surface.

4.2.3 Saturation effects

The previous sections showed how the primary electrons are created, accelerated to the beam pipe due to the bunch interaction, and multiplied as a function of the chamber SEY. However, the electron multiplication is not unlimited. The electron cloud build-up saturates when the electron losses balance the electron generation rate [30]. Depending on the bunch charge, N_b and if multipacting occurs, this can be (roughly) estimated for two regimes :

1. For low bunch charges, saturation takes place when the average neutralization density is reached, i.e. average electric field on the wall is zero. This leads to a linear electron density of

$$\lambda_{\text{sat}} = N_b/s_b, \quad (4.19)$$

where s_b is the distance between bunches.

2. For large bunch charges, saturation occurs when the energy at which the secondary electrons are emitted, $\langle E' \rangle$ is not large enough to penetrate into

the space charge field of the cloud. In this case, the linear saturated density is

$$\lambda_{\text{sat}} = \frac{\pi \langle E' \rangle}{m_e c^2 r_e} \quad (4.20)$$

Note that the first regime shows a direct linear dependence on the bunch population, N_b , while the second does not. The transition occurs at

$$N_{\text{trans}} = \frac{\langle E' \rangle s_b}{m_e c^2 r_e} \quad (4.21)$$

References [30] consider $\langle E' \rangle = E_{\text{sec}}$, independent of the bunch intensity and the bunch spacing. Thus, the conclusion is that if multipacting occurs, the saturated electron density first increases with the bunch population, until it reaches the transition value, above which it stays approximately constant.

4.3 Electron Cloud effects

The presence of EC in the beam chamber can significantly degrade the performance of particles accelerators through different effects [19]:

- **Transverse beam instabilities:** the presence of the EC on the particle beam can drive transverse instabilities. Both “coupled bunch” instabilities and intra-bunch motion [25] can be observed leading to fast transverse emittance blowup and particle losses, which in many cases can prevent a safe operation of the accelerator. Due to the important high frequency content, the conventional transverse feedback systems are usually ineffective in controlling EC induced instabilities.

- **Incoherent beam effects:** the interaction of the beam with the EC can drive incoherent effects as slow emittance blow up, particle losses, transverse tune spread, which are particularly worrying in storage rings and particle colliders where the aim is to store the beam in the ring for a very long time (several hours) while preserving the beam quality.
- **Vacuum degradation:** the electron flux on the chamber's wall stimulates the desorption of gas molecules from the surface which results in an increased residual gas density in the beam chamber, and therefore in a pressure in-crease.
- **Heat load:** the electrons also deposit energy on the chamber's wall. This effect is very important because some accelerator devices operate at cryogenic temperature (e.g the superconducting magnets of the LHC) and the heat load can easily reach the cooling capacity limit of their cryogenic system [26].

4.4 Conditioning and Mitigation

As we have seen, accelerator walls surface properties, like SEY, photon reflectivity and photoelectron yield play an important role in governing EC formation. For these reasons, the knowledge of photo yield and X-ray reflectivity is very important for optimizing ultimate performance at accelerators. Generally countermeasures implemented today are of two kind: active or passive [11, 27]. The first one introduces an external electric or magnetic fields in order to reduce the EC formation, for example:

- **Clearing electrodes** can reduce the electron density around the beam by absorbing or repelling electrons through a static electric field. These kind of

electrodes were tested in KEKB positron ring and a reasonable reduction of the EC was obtained. Nevertheless the presence of electrodes may induce impedance problems and in most accelerator it is not easy to find the space to accommodate them.

- **Solenoids:** implementing weak solenoidal fields it is possible to trap the electrons close to the chamber walls reducing the multipacting effect.

Passive mechanisms, that have been employed at various machines, aim to the reduction of the surface parameters as SEY and Photoelectron Yield and include:

- **Low SEY Coatings:** coat the vacuum chamber with low-emission substances such as TiN, TiZrV or amorphous carbon. It represents the ideal solution to solve most of the EC problems related to the instabilities. An example of this application is the amorphous carbon thin films that have been applied in the CERN SPS (e.g δ_{\max} of amorphous carbon close to 1.0). Experimental results have shown a completely suppression of EC for LHC beam type beams in the liners even after 3 months of air venting and no performance deterioration is observed after more than one year of SPS operation[28].



Figure 4.7: Several mitigation techniques for the EC. Left: Sponge material. Center: Grooves. Right: Clearing Electrodes

- **Geometrical modification:** this idea is based on the fact that electrons contributing to SEY have an energy distribution peaked at very low kinetic energy. Introducing roughness on the surface of chamber like grooves, rough material coating or sponge, there is the possibility that a fraction of secondaries are trapped and can not escape away from the surface. Several studies have been done in this sense, both at CERN and INFN-LNF. In particular, we will analyze the role of the Cu sponge in the Chap. 5.
- **Surface conditioning:** experimental studies have shown that the EC effects in an accelerator can be self-mitigating when the surface of the vacuum chamber is exposed to prolonged electron irradiation. This modification of the material property is called "Electron Scrubbing". It was observed that an electron bombardment from the EC itself can lower the SEY of the chamber walls and gradually reduce the amount of EC. The reduction of the SEY depends on the electron dose which irradiates the surface [19] and stem from a gradual graphitization of the surface.

4.5 EC simulation code: PyECLLOUD

In the past, many of simulations were carried out with the ECLLOUD code, developed and maintained at CERN since 1997. Recently, due to its not modular structure and to the programming language, this code

has been fully reorganized,

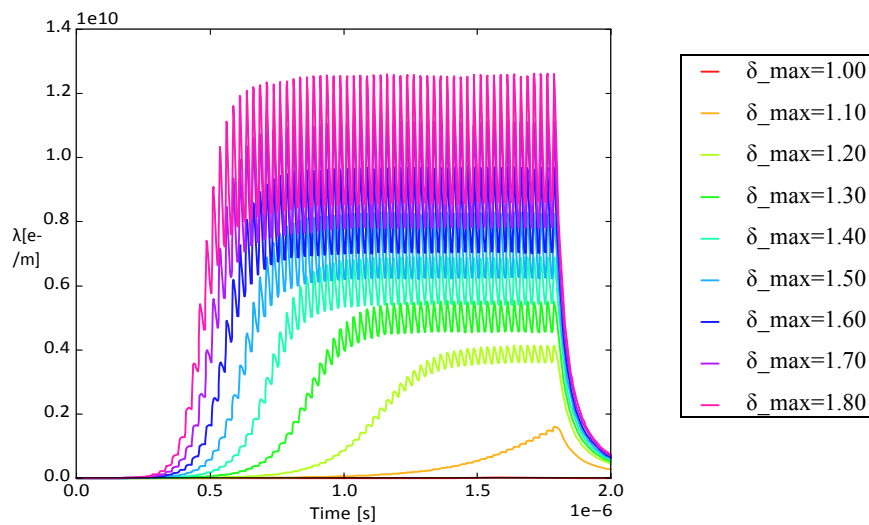


Figure 4.8: Simulated EC build up for different value of δ_{max}

substantial improvements in terms of accuracy, speed and reliability. The new code has been called PyECLoud since it is written in Python and is largely based on the physical models of the ECLoud code.

PyECLoud is a 2D code where the electrons of the cloud are grouped in Macroparticles (MPs) in order to achieve a reasonable computational burden. The beam distribution is assigned *a priori* and it is not affected by Columbian forces from the electrons. With the assumption of "rigid beam", it is possible to study the evolution of the EC but not its effects on the beam.

The dynamics of MP system is simulated following the flow diagram sketched in Fig.4.9 [29]:

- At each time step, a certain number of primary MPs are generated due to residual gas ionization and/or to photoemission in a thin slice around a section of the beam pipe.
- The total electric field acting on each MP is computed as sum of the field

generated by the beam and the space charge field of the electron cloud itself.

The electric field, due to the distributed source, is given by:

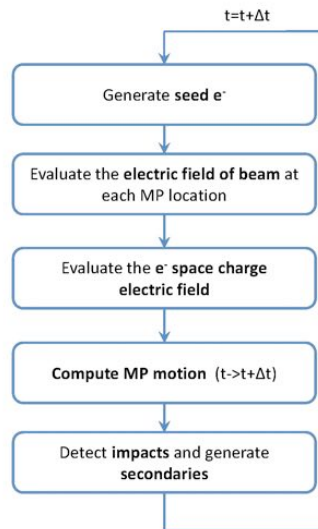


Figure 4.9: Flowchart representing PyECLoud main loop [21]

$$\mathbf{E}(x,y,s,t) = \mathbf{E}_{\perp}(x,y)\lambda(s - ct) \quad (4.22)$$

where $\mathbf{E}_{\perp}(x,y)$ is the transverse electric field, in order to take into account the chamber's profile, it can be evaluated or using the Maxwell's equation or analytically using the Bassetti-Erskine), $\lambda(s - ct)$ is the longitudinal line beam density at the section s at the instant t .

- The space charge contribution is calculated by a classical Particle in Cell (PIC) algorithm, where the finite difference method is employed to solve the Poisson equation with perfectly conducting boundary condition on the beam chamber.

- Once that the total electric field is known, the equations of motion are integrated and the MP positions and momenta are updated accordingly. At this stage the presence of an externally applied magnetic field can also be taken into account.
- At each time step, a certain number of MPs can hit the wall and a secondary emission process is applied to generate emitted electrons.

Since the EC build up can drive an exponential rise of the number of electrons, the MP size is dynamically adapted during the simulation in order to have a computationally affordable number of MPs.

CHAPTER 5

Open Cell Metal Foams for Particle Accelerators

In the CERN Large Hadron Collider [31] a copper-coated stainless steel beam screen (the liner) is kept at ≈ 20 K by active Helium cooling, and effectively handles the heat load represented by synchrotron radiation, photoelectrons, and image-charge losses. A large number ($\sim 10^2 \text{ m}^{-1}$) of tiny slots are drilled in the beam screen wall (see Fig. 5.1) in order to maintain the desorbed gas densities below a critical level (e.g., $\sim 10^{15} \text{ molecules}=\text{m}^3$ for H_2) by allowing desorbed gas to be continuously cryopumped toward the stainless steel cold bore (coaxial to the beam screen) of the superconducting magnets, which is kept at 1.9 K by superfluid helium. Above such critical density levels, nuclear scattering in the residual gas would limit the beam luminosity lifetime, eventually originate high-energy protons which may cause thermal runaway, and ultimately cause quenching of the superconducting magnets. The size, geometry, placement, and density of the pumping slots affect the beam dynamics and stability in a way that is synthetically described by the longitudinal and transverse beam coupling impedances. The slot geometry and placement should be further chosen so as to minimize the effect of trapped (cut off) modes, and to prevent the possible coherent build-up of radiation in the TEM waveguide limited by (the outer surface of) the pipe and the cold bore. Open cell conducting foams could be an interesting candidate for materials to help fulfill the above general

requirements in beam screen design. In addition, the surface roughness of conducting foams may help reduce the effective secondary-emission yield (SEY), thus alleviating the electron cloud build-up phenomenon and related instabilities. In this chapter we present a brief review of open cell conducting foams' properties and modelling tools and discuss at a very preliminary level the pros and cons of their possible use in high synchrotron radiation accelerators.

5.1 Open cell metal foams

Open cell metal foams (OCMF) can be produced by vapor (or electro) deposition of metal on an open cell polymer template, followed by polymer burn off, and a final sintering step to densify the ligaments. Alternatively, they can be synthesized by infiltration and casting of molten metal into a solid mold, consisting of packed (nonpermeable) templates of the foam pores, followed by burnout and removal of the mold. Both processes result in highly gas-permeable reticular materials, where only a 3D web of thin conducting ligaments survives. The typical structure of OCMFs is displayed in Fig.5.2. The key structural parameters of OCMF are the “pore” size and the porosity (volume fraction of pores). Pore sizes in the range from 10^{-4} to 10^{-3} m and porosities in the range 0.7–0.99 are typical. These two parameters determine the gas permeability of the material, and, together with the electrical properties of the metal matrix, its electrical characteristics. OCMF have remarkable structural properties [low density and weight, high (tensile and shear) strength-to-weight ratio, nearly isotropic load response, low coefficient of thermal expansion], as summarized in Table I, which qualified them among the most interesting new materials for aerospace applications. Aluminum and copper OCMF are presently available off the shelf from several manufacturers worldwide, and are relatively

inexpensive. They can be coated, with silver, titanium, or platinum, for special purpose applications.

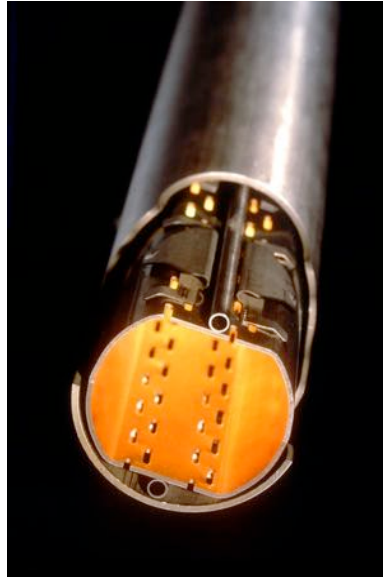


Figure 5.1: The LHC slotted copper-plated beam screen and stainless steel cold bore.

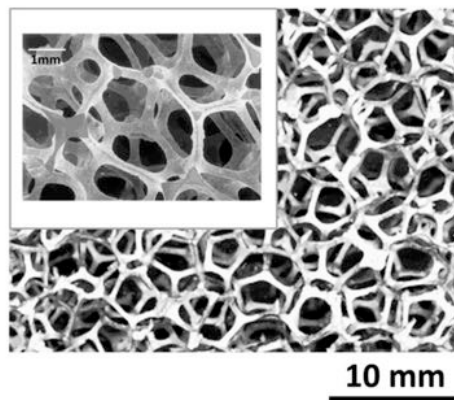


Figure 5.2: A typical open cell metal foam, at two different viewing scales.

Steel and brass foams, as well as silver, nickel, cobalt, rhodium, titanium, or beryllium foams have been also produced.

The Weaire-Phelan (WP) space-filling honeycombs are credited to provide the natural (i.e., Plateau's minimal surface principle compliant) model of OCMF with equally sized (but possibly unequally shaped) pores [32]. The WP unit cell consists of a certain arrangement of (irregular) polyhedra, namely, two pentagonal-face dodecahedra (with tetrahedral symmetry T_h), and six tetrakaidecahedra (with antiprismatic symmetry D_{2d}) featuring two hexagonal and twelve pentagonal faces [32]. A computer generated WP honeycomb is displayed in Fig.5.3, and its visual similarity to Fig.5.2 is apparent.

A powerful open-source cross-platform software project for 3D morphological characterization and modelling of cellular materials, including OCMF, is under development.

	Units	Al	Cu
Compressive strength	[MPa]	2.5	0.9
Tensile strength	[MPa]	1.2	6.9
Shear strength	[MPa]	1.3	1.3
Elastic modulus (compressive)	[MPa]	$1. \times 10^2$	7.3×10^2
Elastic modulus (tensile)	[MPa]	$1. \times 10^2$	$1. \times 10^2$
Shear modulus	[MPa]	$2. \times 10^2$	2.8×10^2
Specific heat	[J=g ⁰ C]	0.89	0.38
Bulk thermal condition	[W=m ⁰ C]	5.8	10.1
Thermal expansion coefficient.	[1= ⁰ C]	2.4×10^{-5}	1.7×10^{-5}
Bulk resistivity	[Ω =m]	7.2×10^{-7}	6.5×10^{-7}
Melting point	[⁰ C]	660	1100

TABLE I. Structural properties of Al and Cu open cell metal foams from.

5.1.1 Electrical properties of conducting foams

Electromagnetic modelling of OCMFs has been thoroughly investigated during the last decade. A numerical approach based on Weiland finite integration technique (FIT, [33]) has been proposed by Zhang et al. [34] to compute the (frequency, thickness, and angle of incidence dependent) reflection coefficient of SiC foam and optimize its design.

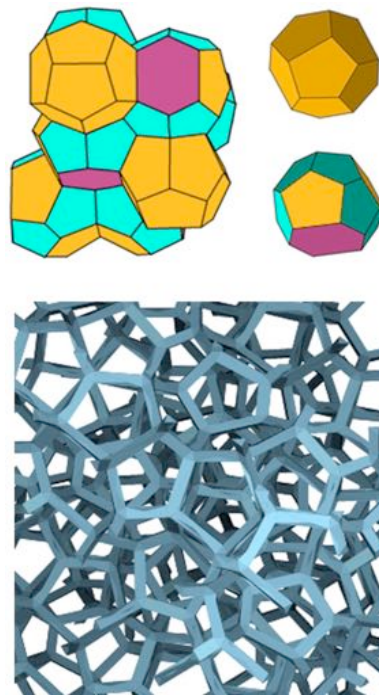


Figure 5.3: The Wearie-Phelan honeycomb cell (top left), its constituent polyhedra (top right), and a numerically simulated reticulated foam thereof (bottom).

The main limitation of Zhang's analysis is in the use of a simple body-centered cubic unit cell foam model, for easiest numerical implementation. The FIT scheme, however, may accommodate more complicated and realistic foam-cell geometries, including in principle the WP one.

In the quasistatic limit $\lambda \rightarrow 0$, the conductivity of OCMFs can be computed using effective medium theory (EMT), for which several formulations exist (see, e.g., [34], [35] for a review). These include (i) the self-consistent approach [36], credited to Bruggemann, where inclusions are thought of as being embedded in the (actual) effective medium; (ii) the differential scheme, whereby inhomogeneities are incrementally added to the composite,¹ until the final concentration is reached, so that at each step the inclusions do not interact and do not modify the field computed at the previous step [37]; and (iii) the effective field methods, whereby interaction among the inclusions is described in terms of an effective field acting on each inclusion, accounting for the presence of the others. Two main versions of this method exist, credited to Mori-Tanaka [38] and Levin-Kanaun [39], differing in the way the effective field is computed (average over the matrix only, or average over the matrix and the inclusions, respectively). The self-consistent approach yields

$$\sigma_{\text{eff}} = \sigma_0(1 - \rho\psi) \quad (5.1)$$

where σ_0 is the bulk metal conductivity, ρ is the porosity (volume fraction of the vacuum bubbles), and ψ is a morphology-dependent factor. The differential approach yields

$$\sigma_{\text{eff}} = \sigma_0(1 - \rho)^\psi \quad (5.2)$$

while the Mori-Tanaka/Levin-Kanaun approaches yield

$$\sigma_{\text{eff}} = \frac{\sigma_0}{(1 + \rho\psi/(1 - \rho))} \quad (5.3)$$

All equations (5.1)–(5.3) merge, as expected, in the $\rho \rightarrow 0$ limit. The above models are synthetically compared to measured values of the static conductivity in Fig. 5.4,

¹ In this approach, the total concentration of inhomogeneities does not coincide with the volume fraction ρ , because at each step new inclusions may be placed where old inclusions have already been set.

for aluminum foams. For aluminum foams, all of these models predict larger conductivity than observed in measurements.² This has been attributed to significant oxide formation on the solid web [40]. Equation (5.2) agrees in form with predictions based on percolation theory [41], although strictly speaking there is no threshold here beyond which the conducting component disconnects.

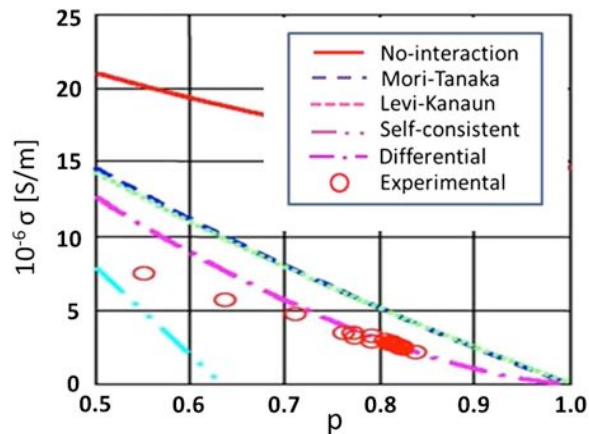


Figure 5.4: Static conductivity vs porosity for aluminum based foams from different EMT models. Measured values are also shown (adapted from [23]).

Measurements of the microwave electromagnetic shielding efficiency of OCMF panels indicate that a simple Drude model

$$\sigma(\omega) = \frac{\omega_p^2 \epsilon_0}{i\omega + \nu} \quad (5.4)$$

² It should be noted that open and closed cell metal foams behave similarly in terms of electrical conductivity, while being markedly different in regards to thermal conductivity, due to the different role of convective flow.

provides a good description of the frequency-dependent conductance of metallic foams. Typically, the relevant plasma and collision frequencies, ω_p and ν , are of the order of a few tens of GHz and a few tens of KHz, respectively. These are notably much smaller³ than their solid metal counterparts (typically in the PHz and GHz ranges, respectively).

OCMF impedance and skin depth

Throughout a typical beam current frequency spectrum, OCMF and bulk metals behave quite differently.⁴ In bulk metals, $\omega \ll \nu \ll \omega_p$ so that the characteristic impedance Z_m and (complex) propagation constant \tilde{k}_{ml} can be written

³ In the light of the well-known formula

$$\omega_p^2 = \frac{N_e q^2}{m_e \epsilon_0}$$

this can be explained as due to a reduction of the electron density N_e , roughly by a factor $(1 - p)$, p being the porosity and a parallel (large) increase of the effective electron mass. Pendry et al. have shown that the effective mass of an electron in a thin-conducting-wire lattice or web is essentially set by its electromagnetic momentum, yielding [25]

$$\omega_p^2 \sim \frac{c^2}{D^2 \log(D/d)}$$

where d and D are the typical conducting-ligament and pore diameters, respectively, and

$$\nu \sim \frac{\epsilon_0 \omega_p^2}{\pi \sigma_0} \left(\frac{D}{d} \right)$$

⁴ The typical power spectrum of a bunched beam in a ring collider consists of lines at integer multiples of f being the bunch spacing, with an envelope approximately $\propto \cos$. In the LHC the -20 dB bandwidth is ~ 1 GHz, roughly 10^5 times the circulation frequency ω_r , and 10^{-1} times the cutoff frequency of the lowest waveguide mode of the beam screen [27]

$$Z_m \sim \frac{1+l}{\sqrt{2}} \left(\frac{\omega v}{\omega_p^2} \right), \quad \widetilde{k}_m \sim \frac{1-l}{\sqrt{2}} k_0(\omega_p) \sqrt{\frac{\omega}{v}} \quad (5.5)$$

Z_0 and $k_0(\omega)=\omega/c$ being the vacuum characteristic impedance and propagation constant, respectively. It is seen that in metallic conductors, both Z_m and \widetilde{k}_m are $\propto \omega^{1/2}$.

In OCMFs, on the other hand, $v \ll \omega \ll \omega_p$ throughout the beam current spectrum, so that the material exhibits a plasmonic behaviour. The OCMF wall (characteristic) impedance Z_f and (complex) propagation constant \widetilde{k}_f are thus given (to lowest order in the small quantities v/ω and ω/ω_p) by

$$Z_f \sim Z_0 \left(\frac{v}{2\omega v} + l \frac{\omega}{\omega_p} \right), \quad \widetilde{k}_f \sim k_0(\omega_p) \left(\frac{v}{2\omega} - l \right) \quad (5.6)$$

Hence, the OCMF characteristic resistance $R_f = \text{Re}[Z_f]$ and skin depth δ_f are both frequency independent, and, e.g., for the case of high-grade ($\rho \approx 5.5 \times 10^{-10} \Omega\text{cm}^{-1}$ at 20 K) copper foam with $p = 0.9$, both fairly small:

$$R_f \sim \frac{Z_0}{2} \frac{v}{\omega_p} \approx 1.4 \times 10^{-5} \Omega, \quad \delta_f \sim \frac{c}{\omega_p} \approx 6 \times 10^{-4} \text{ m} \quad (5.7)$$

The OCMF characteristic reactance

$$X_f = \text{Im}[Z] \sim l Z_0 \frac{\omega}{\omega_p} \quad (5.8)$$

on the other hand, is large compared to that of bulk metal, and grows linearly with ω . For the case, e.g., of high-grade copper foam with $p = 0.9$, $X_f \approx 0.5 \Omega$ at 10^4 Hz.

5.1.2 Superconducting foams

At the operating temperature of the LHC beam screen (~ 20 K), both aluminum and copper exhibit a fairly large conductivity ($\sim 10^7 \Omega^{-1} \text{cm}^{-1}$), but neither of them is superconducting.

Superconducting OCMFs have been discussed in. Foamed ceramic superconductors [in particular, YBCOs (yttrium, barium, copper, oxide)], with critical temperature well above 20 K [high-temperature superconductors (HTS)] have also been already manufactured. These materials may likely exhibit a very low SEY.

Besides being technologically appealing, HTS foams are conceptually interesting materials, where a percolating electric current coexists with a percolating magnetic flux. A substantial body of experimental results on the electrical properties of thin-film HTS is available, and these are reasonably well accounted for by a simple two-fluid Drude model. However, the electrical properties of foamed HTS have been investigated so far, to the best of our knowledge mostly at very low frequencies.

5.2 METAL FOAM vs PERFORATED METAL PATCHED PIPES

In this section we shall attempt to draw a comparison between beam screens using perforated metal patches for outgassing vs pipes using OCMF patches, in terms of the relevant vacuum and beam coupling impedance features.

5.2.1 Vacuum issues

The vacuum dynamics for each molecular species that may be desorbed from the wall by synchrotron radiation can be described by the following set of (coupled) rate equations [42]:

$$\begin{cases} V \frac{dn}{dt} = q - an + b\Theta \\ F \frac{d\Theta}{dt} = cn - b\Theta \end{cases} \quad (5.9)$$

Here $n[\text{m}^{-3}]$ and $\Theta[\text{m}^{-2}]$ are the volume and surface densities of desorbed particles, respectively, and V and F represent the volume and wall area of the beam screen per unit length, respectively.

The first term on the right-hand side of the first rate equation represents the number of molecules desorbed by synchrotron radiation per unit length and time, and is given by

$$q = \eta \Gamma \quad (5.10)$$

where η is the desorption yield (number of desorbed molecules per incident photon) and Γ is the specific photon flux (number of photons hitting the wall per unit length and time).

The second term represents the number of molecules that are removed per unit time and unit length by either sticking to the wall or escaping through the pumping holes and slots. The a coefficient in (5.9) can accordingly be written

$$a = \frac{\langle v \rangle}{4} (s + f) F \quad (5.11)$$

V	liner volume (per unit length)	$1.3 \times 10^{-3} \text{ m}^3/\text{m}$
F	liner surface (per unit length)	$0.14 \text{ m}^2/\text{m}$
η	desorption yield	5×10^{-4}
Γ	photon flux (200 mA beam)	$3.14 \times 10^{16} \text{ s}^{-1} \text{ m}^{-1}$
s	sticking probability	0.6
κ	recycling coefficient	$5. \times 10^{-21} \text{ m}^2$
ν_0	vibrational frequency	10^{13} s^{-1}
W	activation energy	$0.035 \text{ eV/molecule}$

TABLE II. Typical values of the parameters in (5.14) from [42].

where $\langle v \rangle \approx (8kT/\pi m)^{1/2}$ is the average molecular speed, m being the molecular mass, k the Boltzmann constant and T the absolute temperature, $\langle v \rangle/4$ is the average number of collisions of a single molecule per unit time and unit wall surface, s is the sticking probability, and f is the escape probability. The third term accounts for thermal or radiation induced recycling of molecules sticking at the walls. The b coefficient in (5.9) can accordingly be written

$$b = k\dot{\Gamma} + Fv_0 \exp\left(-\frac{W}{kT}\right) \quad (5.12)$$

Here the first term accounts for radiation induced recycling, described by the coefficient $\kappa[\text{m}^2]$, while the second term describes thermally activated recycling, v_0 being a typical molecular vibrational frequency and W a typical activation energy. The $b\Theta$ term appears with reversed sign on the righthand side of the second rate equation, where it represents the number of molecules desticking from the wall surface per unit time and unit length. The first term on the righthand side of this equation represents the number of molecules sticking to the wall, per unit time and unit length, when [compare with Eq. (5.11)]

$$c = \frac{\langle v \rangle}{4} sF \quad (5.15)$$

At equilibrium, $\dot{n} = \dot{\Theta} = 0$, and the rate equations yield

$$\left\{ \begin{array}{l} n_{eq} = \frac{4\eta\dot{\Gamma}}{\langle v \rangle fF} \\ \Theta_{eq} = \frac{s}{f} \frac{\dot{\Gamma}\eta}{k\dot{\Gamma} + Fv_0 \exp\left(-\frac{W}{kT}\right)} \end{array} \right. \quad (5.16)$$

Typical values (for LHC) of the parameters in (5.14) are collected in Table II [42]. The equilibrium molecular densities in (5.14) should not exceed some critical values for safe operation [42].

Beam screen with perforated metal patches

For a beam screen wall with vanishing thickness the molecular escape probability f in (5.11) and (5.14) will be given by the holey fraction ξ_h of the total wall surface. The desorption yield η and the sticking probability s will likewise differ from those of solid metal by a factor $(1 - \xi_h)$.

For a thick perforated wall, the escape probability will be $f = \chi \xi_h$ where the factor $\chi < 1$ (named after Clausing), takes into account the possibility that molecules may stick at the hole internal surface rather than escaping outside.

If only a fraction ξ_p of the beam screen surface is covered by perforated patches, the beam screen escape probability will be $f = \xi_p \chi \xi_h$.

In the LHC the pumping holes are thin slots parallel to the pipe axis. The slots are confined to four narrow (≈ 9 mm wide) strip-shaped patches, running parallel to the pipe axis, as seen in Fig.5.1 The escape probability of an LHC-like slotted patch (strip) is displayed in the left panel of Fig.5.5 Stiffness requirements set a lower limit to the axial (s_L) and transverse (s_T) slot spacings at roughly twice the slot width w . In Fig.5.5 we assume $s_T = 2w$ and plot the escape probability vs the scaled longitudinal slot separation $s_L/2w$, for three typical values of the slots height-to-width ratio h/w . The wall thickness Δ is assumed as equal to w , yielding a Clausing factor $\chi \approx 0.68$.

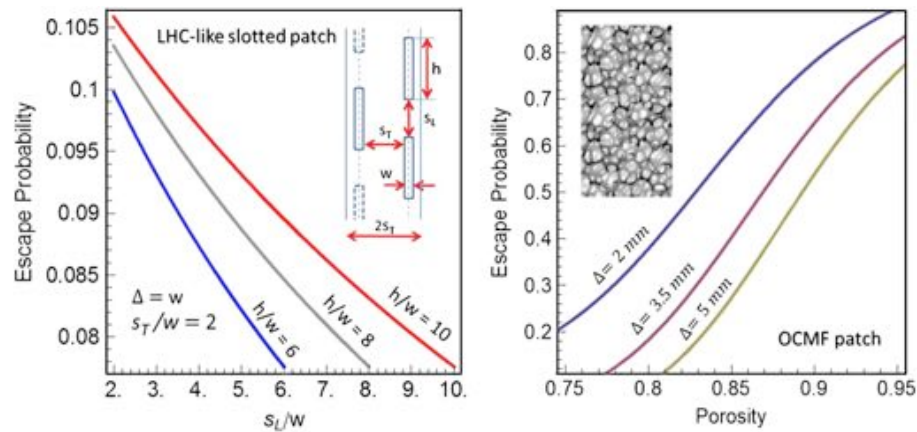


Figure 5.5: Left: escape probabilities for LHC-like slotted patches. Right: escape probability for OCMF patches.

In the LHC the slotted strips represent roughly one-half of the beam screen surface. The slots are ≈ 8 mm long, on average, and ≈ 1.5 mm wide, with $s_L \approx s_T \approx 3$ mm. The holey fraction of the total beam screen surface is roughly 5%, and the escape probability is $\approx 3.5\%$.

Beam screen with OCMF patches

Gas permeability of OCMFs in the molecular flow regime is described by Knudsen diffusivity. The dependence of this latter on foam porosity was fitted numerically in and, using computer simulations of molecular diffusion based on tomographic data of actual OCMF specimens. An exponential blow-up of Knudsen diffusivity D_K was observed, above some porosity threshold, possibly due to the creation of long-range molecular pathways.

From Knudsen diffusivity the escape probability of OCMF patches can be readily obtained, using Fick's (diffusion) law, and is displayed in Fig.5.5 (right panel) as a function of porosity, for different values of the OCMF wall thickness Δ .

It is seen from Fig.5.5 that typical OCMF patches, e.g., with $p = 0.9$, feature fairly

OCMF walls are also expected to provide better EM shielding compared to slotted ones. Hence, gas molecules sticking inside the foam pores will be less exposed to recycling, resulting in possibly smaller values of the recycling factor κ in (5.12) and (5.14).

5.2.2 Beam coupling impedance and parasitic losses

Beam coupling impedances provide a synthetic description of the electromagnetic beam pipe interaction. Here, for the sake of brevity, we shall confine our discussion to the longitudinal impedance. The absolute value and the imaginary part of the latter are inversely proportional to the threshold currents for (single-bunch) microwave instability and Landau damping suppression, respectively, and hence quite relevant to beam stability, while the real part determines the parasitic loss (energy lost by the beam per unit pipe length), via

$$\Delta\varepsilon = \frac{1}{2\pi} \int_{-\infty}^{\infty} |I(\omega)|^2 \text{Re}[\bar{Z}_{\parallel}(\omega)] d\omega \quad (5.15)$$

where $I(\omega)$ and $Z_{\parallel}(\omega)$ are the beam current spectrum and longitudinal impedance per unit length, respectively.

The following relationship exists (to first order in the wall impedance) between the longitudinal impedance per unit length \bar{Z}_{\parallel} of a patched-wall beam screen and the (known) longitudinal impedance per unit length $\bar{Z}_{\parallel}^{(0)}$ of the same pipe with a perfectly conducting wall

$$\bar{Z}_{\parallel} = \bar{Z}_{\parallel}^{(0)} + \frac{\varepsilon_0 \gamma_0}{c\lambda^2} \oint_{\partial S} Z_w(s) |E_{0n}(s)|^2 ds, \quad (5.16)$$

where Z_w is the (local) Leontóvich impedance of the patched wall, ∂S is the pipe cross-section contour, $Y_0 = (\epsilon_0 = \mu_0)^{1/2}$ the vacuum admittance, Λ the beam linear charge density, and $E_n^{(0)}$ the (known) field component normal to the pipe wall in the perfectly conducting pipe.⁵ According to (5.16), perforated or slotted or OCMF patches placed where the normal field component $E_n^{(0)}$ is minimal will have minimum impact on the longitudinal impedance. Hence, a circular beam screen, featuring a uniform field along ∂S , represents the worst case, where the longitudinal (and transverse) beam coupling impedances are simply proportional to the average of the wall impedance, assumed as piecewise constant

$$\langle Z_{wall} \rangle = \sum_i \xi_i Z_{wall}^{(i)} \quad (5.17)$$

ξ_i being the surface fraction covered by patches with wall impedance $Z_{wall}^{(i)}$.

Impedance of perforated patch

The effective wall impedance of a perforated patch can be computed under the Bethe approximation where the holes and slots are (much) smaller than the shortest wavelength in the beam spectrum, yielding [43], [44]

$$Z_s^{(0)} = l Z_0 \left(\frac{\omega}{c} \right) a_{tot}^{(i)} n_\sigma \quad (5.18)$$

$Z_0 = (\mu_0 / \epsilon_0)^{1/2}$ being the vacuum characteristic impedance, $a_{tot}^{(i)}$ the total internal polarizability of the holes and slots, and n_σ their surface density.

In [45] the more general case, relevant for the LHC, of a circular perforated beam screen with inner radius a and thickness Δ surrounded by a circular coaxial lossy tube (the cold bore) with radius b was investigated.

⁵ A similar formula exists for the (dyadic) transverse impedance [41].

It was found that the beam screen wall impedance can still be cast in the form of Eq. (5.18), after the formal substitution

$$a^{(i)} \rightarrow a^{(i)} + Fa^{(e)} \quad (5.19)$$

where the superfix (e) identifies the total external polarizability of the holes and slots in a wall with thickness Δ , and [44], [45]

$$F = -\frac{a^{(e)}}{a^{(i)}} \left[1 + l \left(1 + \frac{b}{a+\Delta} \right) \frac{Z_{cb}}{Z_h^{(0)}} \right]^{-1} \quad (5.20)$$

Z_{cb} being the cold bore wall impedance.⁶ The wall reactance is negligibly affected by the presence of the external tube, which produces a small resistive component, accounting for radiation leakage through the slots.

	Solid copper patch	OCMF patch	OCMF roughness	Slotted patch (perfect conductor)
$(\omega_R/\omega)R_{wall}; [\Omega]$	$4.9 \times 10^{-6} \sqrt{\omega_R/\omega}$	$1.4 \times 10^{-5} (\omega_R/\omega)$	0	$1.0 \times 10^{-13} \sqrt{\omega/\omega_R}$
$(\omega_R/\omega)X_{wall}; [\Omega]$	$4.9 \times 10^{-6} \sqrt{\omega_R/\omega}$	5.5×10^{-5}	5.5×10^{-6}	3.1×10^{-7}

TABLE III. Summary of Leontóvich impedances. High-grade copper with $\rho \approx 5.5 \times 10^{-10} \Omega \text{cm}^{-1}$ at 20 K. OCMF with 1 mm pores and 0.1 mm ligaments. Slots in a perfectly conducting wall as in Fig. 5, with $w = \Delta = 1.5$ mm, $h = 10w$, and $s_T = s_L = 2w$.

⁶ In this formula Z_{cb} is the impedance of both the the cold bore and outer beam screen walls.

external tube, which produces a small resistive component, accounting for radiation leakage through the slots. We use the following formulas from for thin axial slots from [46].

$$\begin{aligned}
 a_{tot}^{(0)} &= w^3 \left(0.1334 - \frac{0.005w}{h} \right) \\
 a_{tot}^{(i)} &= \left(\frac{8}{\pi^2} \right) a_{tot}^{(0)} \\
 a_{tot}^{(e)} &= \exp \left(-\frac{\pi\Delta}{w} \right) a_{tot}^{(0)}
 \end{aligned} \tag{5.21}$$

where $a_{tot}^{(0)}$ is the total polarizability of a slot in a vanishingly thin wall, and all other symbols are defined in Fig. 5.5.

Impedance of OCMF patch

A straightforward solution, which is not included for brevity, of the electromagnetic boundary value problem for a (relativistic, vanishingly thin) axial beam in a circular OCMF beam screen, with radius a and thickness Δ surrounded by a coaxial (infinitely thick) conducting circular tube (the cold bore) with radius $b > a + \Delta$ shows that if Δ exceeds a few skin depths δf across the whole beam current spectrum, which is certainly the case here, as seen from Eq. (5.7), the Leontóvich impedance of the OCMF beam screen wall is fairly well approximated by the intrinsic impedance of the OCMF, viz., [cf. Eq (5.6)]

$$Z_f = Z_0 \left(\frac{v}{2\omega_p} + l \frac{\omega}{\omega_p} \right) \tag{5.22}$$

The surface roughness of the foam also contributes to the OCMF wall impedance. The order of magnitude of this contribution can be estimated from [47].

$$Z_f^{(rough)} \approx l \sqrt{\frac{\pi}{32}} Z_0 \left(\frac{h}{L}\right) \frac{\omega}{c} h \quad (5.23)$$

h and L being the rms height and correlation length of the surface roughness, respectively.

Impedance budget

For illustrative purposes, the numerical values of the real and imaginary components of the relevant wall impedances, normalized to the mode number [i.e., multiplied by the $(\omega R = \omega)$ factor], have been collected in Table III. Here we assume high-grade copper ($\rho \approx 5.5 \times 10^{-10} \Omega \text{cm}^{-1}$ at 20 K) for the solid, slotted, and foam-matrix metal. The numbers in Table III for the slotted patch are obtained for the slot geometry depicted in Fig. 5.5, with $w = \Delta = 1.5$ mm, $h = 10w$, and $sT = sL = 2w$, for which $\xi h \approx 0.14$, and the escape probability reaches its fiducial upper limit $f \approx 0.1$. The numbers for the foamed patch are obtained assuming a typical pore diameter ~ 1 mm, and a typical ligament size ~ 0.1 mm, yielding $\omega p \approx 7.93 \times 10^{10} \text{ rad sec}^{-1}$ and $\nu \approx 3.66 \times 10^4 \text{ Hz}$ in the Drude model consistent with typical measured values of the static conductance of open cell copper foams. We assume a typical rms roughness scale $h \approx 0.125$ mm and a correlation length $L \approx 0.25$ mm. As seen from Table III, the copper wall resistance is larger than that of the OCMF up to $\omega = 10^5 \omega_R$. On the other hand, the OCMF wall reactance is relatively large, and exceeds significantly that of a perfectly conducting slotted wall as well as that of solid copper. However, as seen from Fig.5.5, a typical OCMF wall pumping capacity (escape probability) is several times larger than that of the “best” slotted wall. Thus, to

obtain the same pumping capacity, the patched beam screen surface needed in the OCMF case is only a small fraction of that for the slotted case. This makes it easier to place the OCMF patches where the (unperturbed) field in Eq. (5.16) is minimal, so as to minimize their impact on the beam coupling impedance.

5.2.1 Secondary emission yield

Perforations reduce the secondary emission yield of a metal wall by a factor roughly proportional to the solid fraction of the surface.

The SEY of metals is strongly reduced by surface roughening, obtained, e.g., by powder blasting. For the special case of periodic rectangular grooves etched on a flat metal surface, the SEY dependence on the groove depth-to-spacing and width-to-thickness ratios has been investigated, indicating that larger ratios yield a smaller SEY [48].

Carbon coating also reduces SEY effectively [49], at the expense of some increase in wall resistance.

It is reasonable to expect that OCMFs may exhibit a much lower SEY compared to solid metals in view of their random like surface roughness. The SEY of an OCMF wall will depend on the effective roughness of its surface, which is a function of the foam porosity and average pore size. OCMF surface roughness, however, should be kept small enough, to prevent the blow-up of wall reactance. No measurements of the SEY of OCMFs are available yet, to the best of our knowledge, but should be straightforward [50].

CHAPTER 6

Open Cell Metal Foams: Measurement and Numerical results

MU-EPSSLN™ is a high performance software package to do one and two port coax and waveguide measurements using computers running Microsoft Windows™ or Apple Intel Macintosh operating systems. For the best measurements, samples must be homogeneous and fit the sample holders tightly. For coax, this means that the sample must have uniform contact with both center and outer conductors; for waveguide, the samples must have uniform contact with the broad walls of the waveguide (the contact with the narrow walls is important, but it is less critical).

6.1 General Description of MU-EPSSLN™

The MU-EPSSLN™ is a complete software package for making S-parameter measurements using one and two port coax or waveguide fixtures. Data reduction routines to calculate the complex permeability (μ) and permittivity (ϵ) of materials as well as other parameters are provided. The program does all the instrument control and real time data processing. The user has access to all raw and processed data to allow for additional and/or custom data processing. User selected bands can be swept using as few as 3 or as many as 1601 frequencies (depending on analyzer).

All the capabilities of the network analyzer are available to the user either through the external controller or the front panel. Complex μ and ϵ are normalized relative to free space parameters μ_0 and ϵ_0 . They are defined by the expressions $\mu = \mu' - j\mu''$ and $\epsilon = \epsilon' - j\epsilon''$ where μ'' and ϵ'' are non-negative real numbers and where the complex time dependence in the relevant field equations is of the form $e^{+j\omega t}$. The algorithms used to obtain these parameters are based upon the cited references. Although the model that solves for both μ and ϵ , frequency by frequency, is not the Nicolson-Ross Model, it has the same half wavelength problem as do all such models. For purely dielectric materials ($\mu = 1$), the value of ϵ which is obtained from the Eps from Transmission Reduction algorithm is equivalent to the NIST precision reduction when beta = 0. In other words, both algorithms employ transmitted S-parameters only, and thereby avoid half wavelength difficulties. The main reductions of **MU-EPSLN™** are Eps from Transmission, Anisotropic MuEps, Epsilon with Arbitrary Load, MuEp S11, Nicolson-Ross, and Short Free Space .



Figure 6.1: Photos show the **MU-EPSLN™**

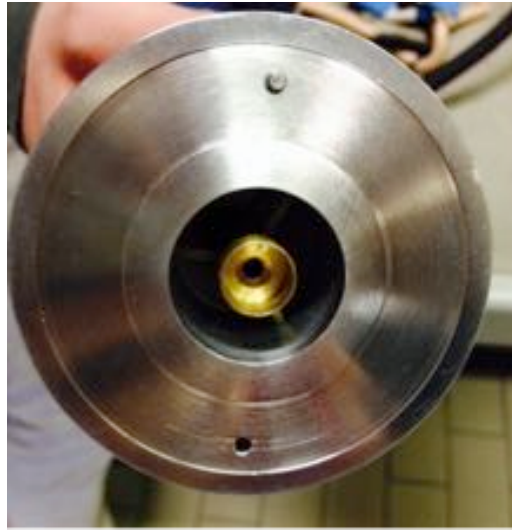


Figure 6.2: The figure shows one port "MU-EPSLN" coaxial line.

6.2 Measurement Theory

One port "MU-EPSLN" coaxial line (Fig.6.2), measurements of material properties are based upon the input impedance of a line of length l , which is loaded with a sample of relative permeability, μ , and relative permittivity, ϵ and which is terminated by a known (measured) load.

When the load is a short, the normalized input impedance is:

$$Z = j \sqrt{\frac{\mu}{\epsilon}} \tan \left(\frac{2\pi f}{c} \sqrt{\mu\epsilon l} \right) \quad (6.1)$$

and, when an open,

$$Z = -j \sqrt{\frac{\mu}{\epsilon}} \cot \left(\frac{2\pi f}{c} \sqrt{\mu\epsilon l} \right) \quad (6.2)$$

Here c is the speed of light and f is the frequency and the input impedance is determined from the measurement of the reflection coefficient ρ ; i.e.

$$Z = \frac{1+\rho}{1-\rho} \quad (6.3)$$

The permeability μ , of magnetic materials may be measured using a short as a load when ϵ is known by means of the first relationship. When the sample is electrically thin, **MU-EPSLNTM** uses the small argument approximation of the tangent function

$$Z = j\mu \frac{2\pi f}{c} l \quad (6.4)$$

The physical interpretation of this quick solution is one of the inductive reactance of the sample.

The permittivity ϵ , of a material also may be measured with a short circuit load when μ is known. For dielectrics, **MU-EPSLNTM** sets μ equal to 1.

For electrically thin samples terminated by an open circuit, **MU-EPSLNTM** approximates the cotangent function and solves for permittivity using the result

$$Z = \frac{c}{j\epsilon 2\pi f l} \quad (6.5)$$

This represents the capacitive reactance of the thin sample.

When neither constitutive parameter is known, **MU-EPSLNTM** solves for μ and ϵ using two short circuit measurements, each with a different thickness. Although these relations are exact for TEM propagation, they are transcendental and permit many valid solutions, only one of which is correct. It is often desirable to use thin

samples (less than one quarter wavelength) so that the first solution is certainly the correct one.

MU-EPSLNTM calculates the free space and short backed reflection and transmission coefficients for a material with arbitrary mu and epsilon at normal incidence. The sample thickness is input by the user. The implementation is based upon a direct analogy of TEM propagation in a coaxial line and a normally incident plane wave propagation in a coaxial line and a normally incident plane wave propagating in free space. Figure 6.3 illustrates the plane wave geometry:

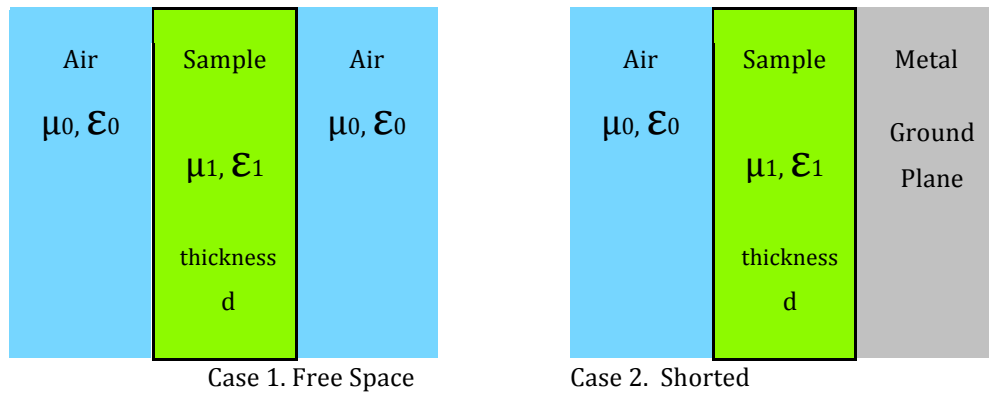


Figure 6.3. Normal Incidence Propagation in Free Space

The solution of this boundary value problem results in the following complex reflection and transmission coefficients:

$$\rho_{fs} = \frac{(1-\eta_1)(1+\eta_1)\exp(-j2\beta_1 d) + (\eta_1-1)(1+\eta_1)}{(1+\eta_1)^2 + (\eta_1-1)(1-\eta_1)\exp(-j2\beta_1 d)} \quad (6.6)$$

$$\tau = \frac{4\eta_1 \exp(-j2\beta_1 d)}{(\eta_1+1)^2 + (\eta_1-1)(1-\eta_1)\exp(-j2\beta_1 d)} \quad (6.7)$$

$$\rho_{sh} = \frac{(1-\eta_1)+(1+\eta_1)\exp(-j2\beta_1 d)}{(\eta_1-1)\exp(-j2\beta_1 d)-(1+\eta_1)} \quad (6.8)$$

where

$$\eta_1 = \sqrt{\frac{\mu_1}{\varepsilon_1}}, \quad \beta_1 = \frac{2\pi\sqrt{\mu_1\varepsilon_1}}{\lambda_0} \quad (6.9)$$

and μ_1 and ε_1 are relative values and η_1 is the characteristic impedance normalized to free space. Similar concepts apply to waveguide and oblique incidence free space measurements.

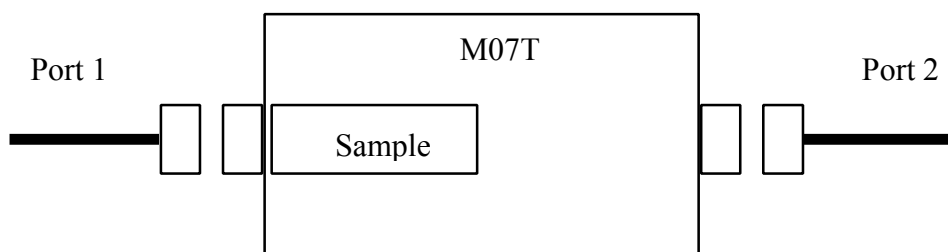
6.3 Software and Measurement procedure

The **MU-EPSLN™** program is a network analyzer controlling program written for measurement platforms such as those furnished by Damaskos, Inc. Data collection, reduction and output are integrated in the Microsoft Windows environment.

Features of the program include selection of one of several network analyzers; ASCII storage of measurement, time domain, permittivity, and permeability data; various data reduction routines; file merging; multiple output plots; multiple plots on screen; thin sheet resistivity, capacitance and inductance; time domain plots; context sensitive help information and raw data manipulation. Five data reductions are provided for computation of permittivity and permeability. The *Epsilon with Arbitrary Load* reduction computes the permittivity of the sample using one reference measurement and one reflection coefficient measurement. The *Epsilon at*

Open computes the permittivity of a thin sample. *Anisotropic Mu Eps*, and *Nicolson-Ross* require a reflection and transmission measurement to compute the permittivity and permeability of the sample. The *Mu at Short* data reduction uses a thin sample approximation to compute the sample permeability measured against a short. A two sample data reduction, *Mu Ep S11*, computes the permeability and permittivity of the material that has been measured at two thicknesses. Solid samples machined to the dimensions of coax fixtures may be slipped over the center conductor and placed anywhere along the conductor; however placement at the ends should be avoided. A tight fit on the center conductor is required for good measurements. Slight oversizing gives good contact to the outer conductor. Oversizing also helps provided good contact to waveguide sample holders (contact with the broad walls is the most important).

Measurement Configuration



6.3.1 Calibration

The first step in making a measurement is to perform a calibration of the network analyzer. This is done from the **MU-EPSLN™** program by selecting an appropriate calibration procedure. In general, TRL/LRL offers the best calibration followed by a

SOLT (Short, Open, Load, and Thru) (Note that SOLT can only be done in coax). Simpler calibrations using just a short or thru may be more practical. Two cables should be used to connect the fixture to the network analyzer. Adaptors can be used to connect the cables to the fixtures. Follow the instructions displayed on the computer screen. Note that for a TRL/LRL calibration the sample holder or a through standard (For Free Space measurements one of the antennas must be moved) is used as the through delay in the calibration and the two adaptor sections are clamped together for the zero length through. Once the calibration is complete it can be stored for later use. Depending on the network analyzer in use, the choices for calibration are *Response*, *Response & Isolation*, *S11 One Port*, *S22 One Port*, *One Path Two Port*, *Full Two Port*, *TRL Two Port*, and *Load Old Calibration*. For a TRL calibration, as an example, select coax or waveguide, enter the short length for the **REFLECT STANDARD** (usually 0.00 cm), then enter the first thru length (usually 0.00 cm), and then enter the **THRU** length of the **THRU DELAY** (the second member of the thru value list; this value is the physical length of the standard).

Frequency Selection

The Frequency Selection dialog box appears during the calibration process. The user may select the start, stop and number of frequencies from the choices shown below. The frequency units may be changed at any time before closing this dialog box. In addition, multiple frequency bands may be entered if the analyzer permits.

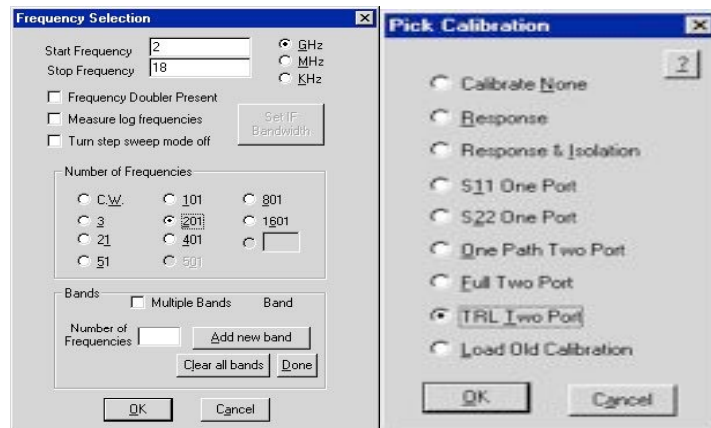


Figure 6.4: Dialog boxes for calibration and frequency selection

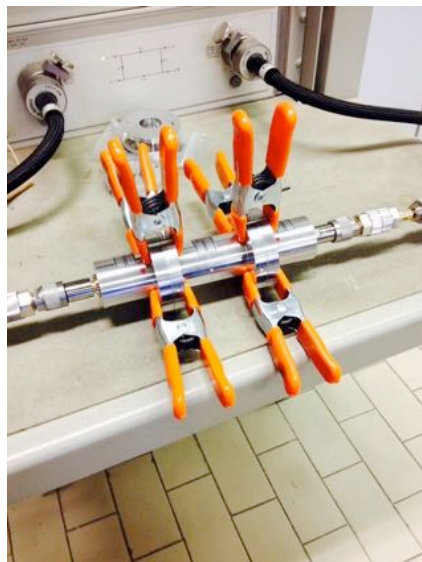


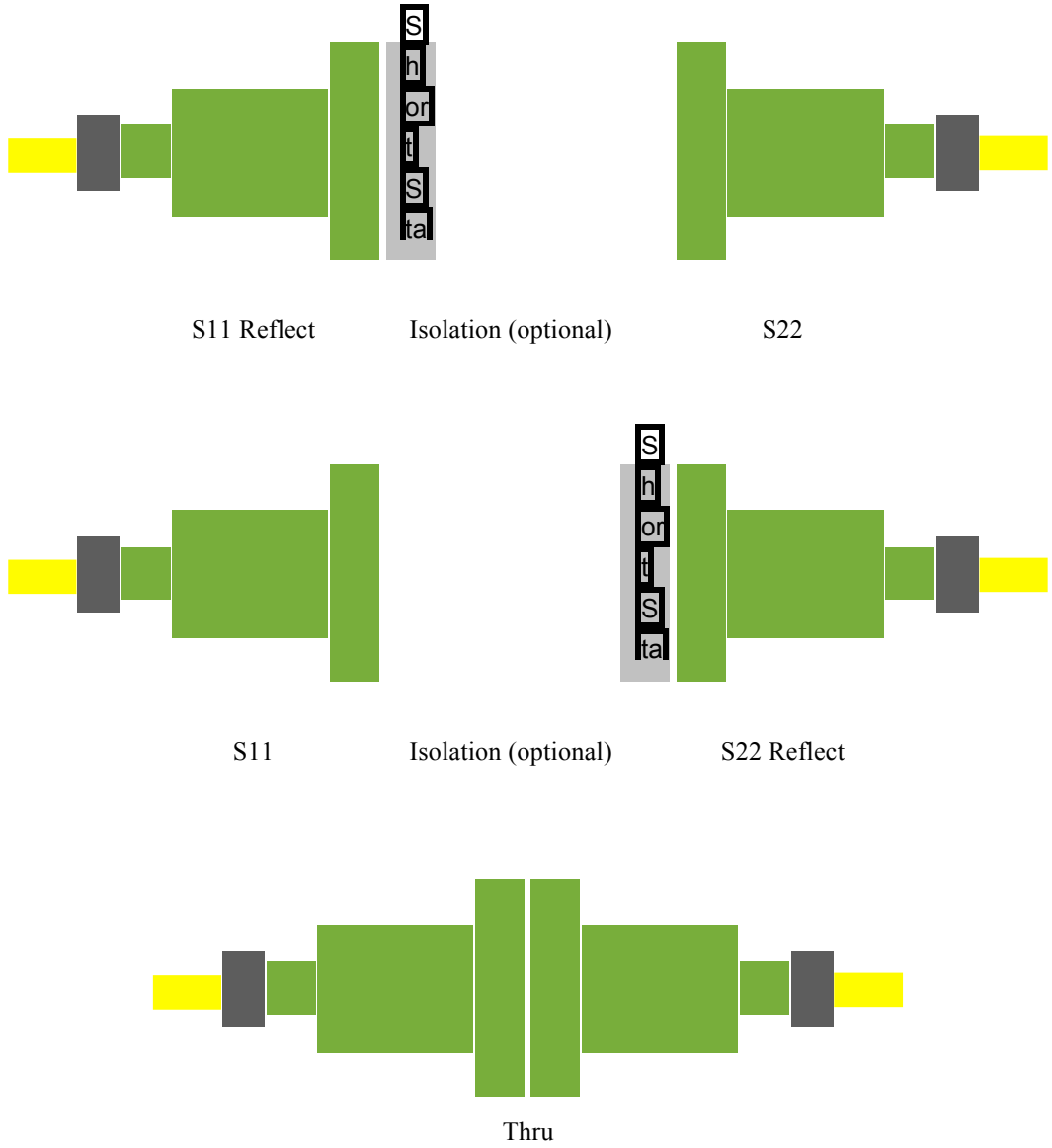
Figure 6.5: The figure shows line calibration

The Thru-Reflect-Line calibration procedure is used when high quality short, open, load and thru standards of a conventional full two-port calibration are not available.

The TRL cal requires identical one port high reflection coefficient standards on each port, a thru measurement with the two ports connected together and a delay measurement with a short length of transmission line between the ports. The

crosstalk (S_{21} & S_{12}) in the test set of the network analyzer may be measured or omitted by selecting the Isolation button.

TRL Calibration Steps



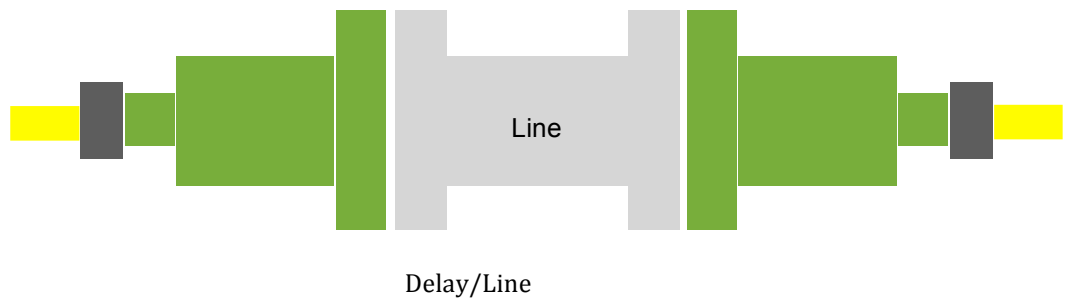


Figure 6.6: Long or Short Standard or Empty Holder with center conductor and ferrules

6.3.2 Data Reduction

Data reductions permitted with the **MU-EPNLN™** program are as follows:

◆ Eps From Transmission

This function uses transmission coefficient data to recover the complex permittivity of the material of known thickness. The material is assumed to have a permeability $1+j0$. The reduction works for both coax data and waveguide data assuming the cut off frequency is known.

◆ Nicolson-Ross

This function is similar to the Anisotropic MuEps but it does not correct data for horn angle. This reduction works best for lossy samples and samples that are less than $\frac{1}{4}$ lambda thick. It does not work well for dielectric samples that are $\frac{1}{2}$ lambda and greater. Dielectric samples, where $\mu = 1$, are best processed with the **Eps from Transmission reduction**.

◆ Anisotropic Mu Eps

This function computes the permeability and permittivity of a sample from TE₁₀ waveguide or coax S-parameter measurements. If the permeability is anisotropic, check the Anisotropic Sample box and enter the complex z-directed permeability component. By selecting one reflection and one transmission coefficient of the measurement, the permeability and permittivity may be determined. Values for sample thickness and sample holder length must be entered as positive values. But the sample offset distance, measured from the reflection plane, may be positive, negative or zero. The electrical thickness estimate, initially set at zero, is changed by clicking on the scroll bar to increase or decrease. If the sample's electrical thickness is less than one quarter wavelength then the setting should be zero. A sample ranging 1/4 to 3/4 lambda should have a setting of 1 etc. If the results do not seem reasonable, then experiment with other estimates.

◆ Epsilon with Arbitrary Load

This function computes the complex permittivity assuming that the permeability is 1-j0. The reduction requires a single reflection coefficient measurement and a reference measurement. The sample is backed by an arbitrary load impedance. The sample offset distance, measured from the reflection plane, may be positive, negative or zero.

◆ Mu at Short (thin sample)

This function allows the user to compute the permeability of magnetic samples measured against a short circuit. It is valid only for electrically thin samples measured in a short circuit coax, waveguide or in free space (TEM). The only parameter required is the sample thickness and the sample permittivity is assumed to be $1+j0$. Note that the reduction assumes that the reflection coefficient has been divided by a short circuit reference that is located immediately behind the sample.

◆ Epsilon at Open (thin sample)

This function allows the user to compute the permittivity of thin dielectric samples measured at an open circuit. It is valid only for electrically thin samples. The only parameter required is the sample thickness and the sample permeability is assumed to be $1-j0$. Note that the reduction assumes that the reflection coefficient has been divided by an open circuit reference that is located immediately behind the sample.

◆ Mu Ep S11 (two samples)

This function uses reflection coefficient data for two different sample thicknesses. It computes the complex permeability and permittivity for the data frequency by frequency. In order for the calculation to be successful both samples must be of homogeneous material and the thicknesses must be different. The reduction works for normal and oblique incidence.

6.4 Measurement's Results

In University of Salerno's laboratory, we have analysed three different types of open cell metal foams:



Figure 6.7: The picture shows the three foams. Left: Aluminium 16. Center: Copper. Right: Aluminium 4.

The characteristics of the three samples can be summarized as follows:

	Aluminium 4	Copper	Aluminium 16
Thickness	6.35 mm	6.35 mm	6.35 mm
Bulk density	0.2g.cm	0.8g.cm	0.2g.cm
Porosity	93%	91%	93%
Pores/cm	4	4	16
Purity	98.5%	99.9%	98.5%
Size	150x150 mm	150x150 mm	150x150 mm
Net weight	37.4 g	114 g	37.4 g

At the beginning, after the calibration, we choose the frequency (0.1-1 GHz) with a range of 51 points. Then, the first measure was performed on Aluminium 4, putting five rings of the foam in the line of our instrument. So, we calculated, starting from the reflection and transmission coefficients,

$$\Gamma = \frac{Z_{mat} - Z_0}{Z_{mat} + Z_0} \quad (6.10)$$

Where :

$$Z_{\text{mat}} = \sqrt{\frac{\mu_{\text{mat}}}{\varepsilon_{\text{eq}}}}, \quad \varepsilon_{\text{eq}} = \varepsilon_0 \varepsilon_r = \varepsilon_0 + \frac{\sigma}{j\omega} \quad (6.11)$$

the permittivity (ε):

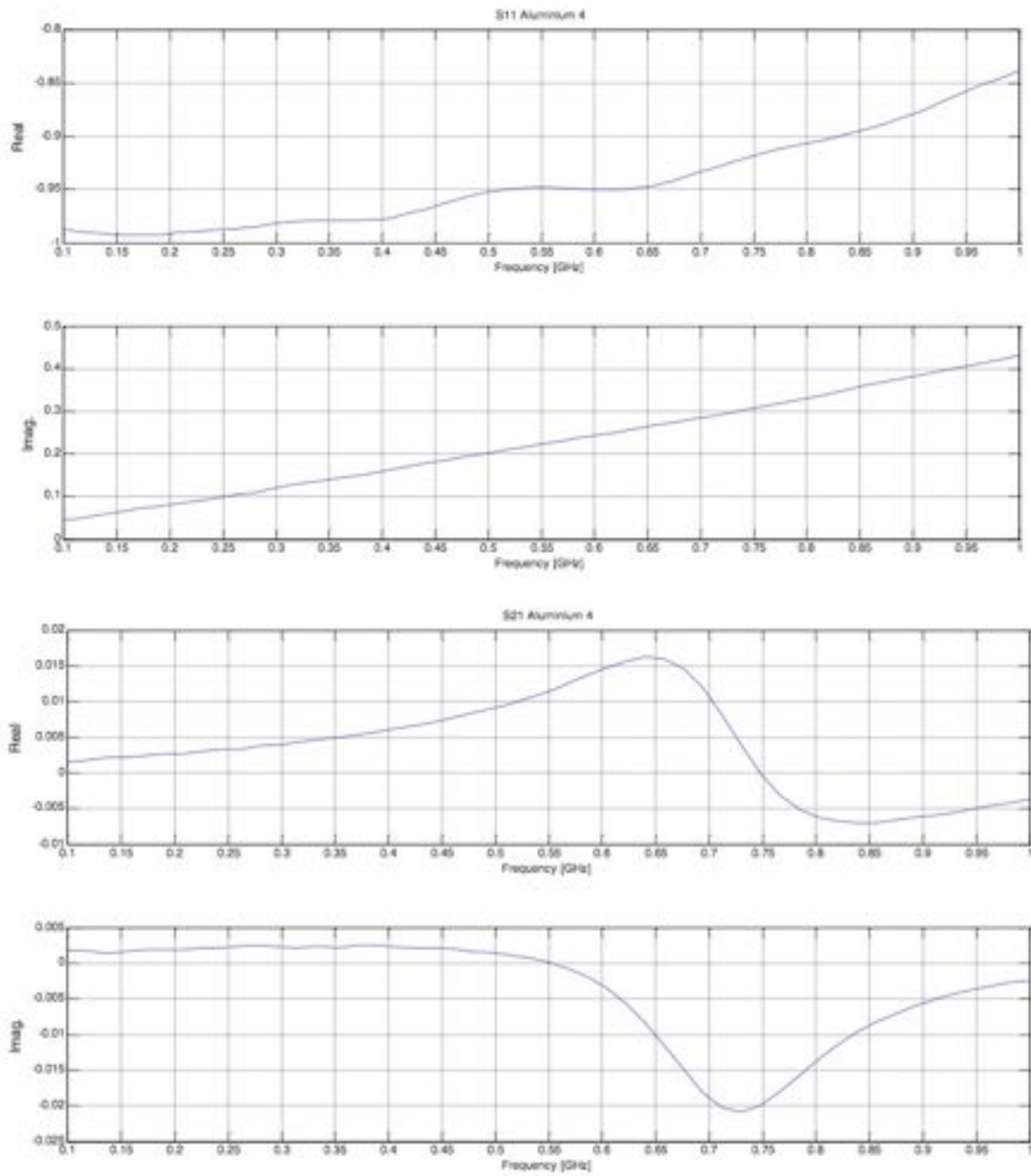
$$\varepsilon_r = \frac{(1-\Gamma)^2}{(1+\Gamma)^2} \quad (6.12)$$

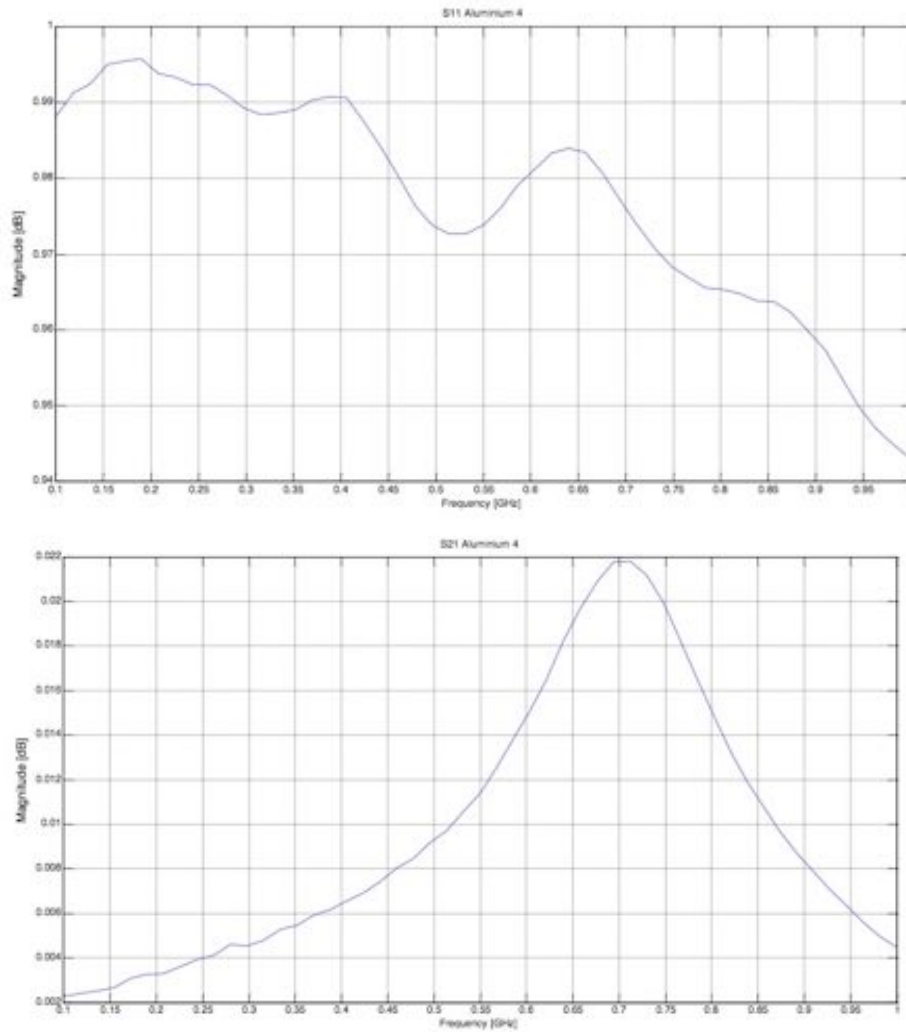
The data related to the reflection and transmission coefficients for the porte one are:

S ₁₁			S ₂₁		
Freq [GHz]	Real	Imag.	Freq [GHz]	Real	Imag.
0.1	-0.987122	0.0449219	0.1	0.00147599	0.00171655
0.118	-0.990021	0.0506592	0.118	0.00172406	0.00170052
0.136	-0.990845	0.0575256	0.136	0.00212669	0.00135183
0.154	-0.992981	0.0645142	0.154	0.00211155	0.00163853
0.172	-0.992828	0.0725708	0.172	0.0024488	0.00188875
0.19	-0.992737	0.0781555	0.19	0.00269365	0.00183225
0.208	-0.990356	0.0832825	0.208	0.00268388	0.00190032
0.226	-0.989288	0.0895996	0.226	0.00296843	0.00208616
0.244	-0.987732	0.0963135	0.244	0.00329721	0.0021323

0.262	-0.986755	0.105316	0.262	0.00330138	0.00243831
0.28	-0.985046	0.108948	0.28	0.00383949	0.00257587
0.298	-0.981995	0.120178	0.298	0.00395417	0.00224566
0.316	-0.980194	0.127136	0.316	0.00424981	0.00219464
0.334	-0.979492	0.134094	0.334	0.00466871	0.00243092
0.352	-0.979065	0.140472	0.352	0.00499916	0.00215983
0.37	-0.97937	0.147217	0.37	0.00537252	0.00247455
0.388	-0.978638	0.15448	0.388	0.00565314	0.00245786
0.406	-0.977356	0.162262	0.406	0.00615954	0.00228357
0.424	-0.972778	0.170563	0.424	0.00653648	0.00219226
0.442	-0.967804	0.178223	0.442	0.00712991	0.00213861
0.46	-0.962616	0.185516	0.46	0.00778198	0.00203037
0.478	-0.957214	0.192993	0.478	0.00832367	0.00166655
0.496	-0.953033	0.200378	0.496	0.00905085	0.00151873
0.514	-0.950195	0.208252	0.514	0.009655	0.00114107
0.532	-0.948456	0.215881	0.532	0.0105553	0.000734806
0.55	-0.947937	0.223145	0.55	0.0114322	9,58E+00
0.568	-0.948456	0.230591	0.568	0.0125484	-0.000731945
0.586	-0.949799	0.237549	0.586	0.0137315	-0.00194979
0.604	-0.950287	0.244446	0.604	0.0147147	-0.00343752
0.622	-0.950531	0.25174	0.622	0.0155683	-0.00557804
0.64	-0.949005	0.259888	0.64	0.0162392	-0.00829697
0.658	-0.946442	0.26712	0.658	0.0159607	-0.0114527
0.676	-0.941284	0.274658	0.676	0.0146031	-0.0149527

0.694	-0.935425	0.282562	0.694	0.01196	-0.0181723
0.712	-0.929688	0.290161	0.712	0.00814533	-0.0202332
0.73	-0.924072	0.297913	0.73	0.00387383	-0.020812
0.748	-0.918732	0.306213	0.748	-6,48E+00	-0.0199604
0.766	-0.914368	0.314575	0.766	-0.00304413	-0.0180311
0.784	-0.909882	0.323181	0.784	-0.00504684	-0.0157347
0.802	-0.906647	0.331512	0.802	-0.00630665	-0.013494
0.82	-0.902649	0.340912	0.82	-0.00680351	-0.0114198
0.838	-0.898071	0.350189	0.838	-0.00695419	-0.0096941
0.856	-0.893921	0.360291	0.856	-0.00697422	-0.00827789
0.874	-0.888611	0.369568	0.874	-0.00658298	-0.00707984
0.892	-0.881897	0.378784	0.892	-0.0063076	-0.00598383
0.91	-0.875977	0.386444	0.91	-0.00603008	-0.00504684
0.928	-0.867737	0.395264	0.928	-0.00555658	-0.00435328
0.946	-0.860107	0.403046	0.946	-0.00513721	-0.00369716
0.964	-0.852173	0.412933	0.964	-0.00463963	-0.0031507
0.982	-0.845856	0.421143	0.982	-0.00417352	-0.00270653
1	-0.838531	0.431458	1	-0.00376368	-0.0024091





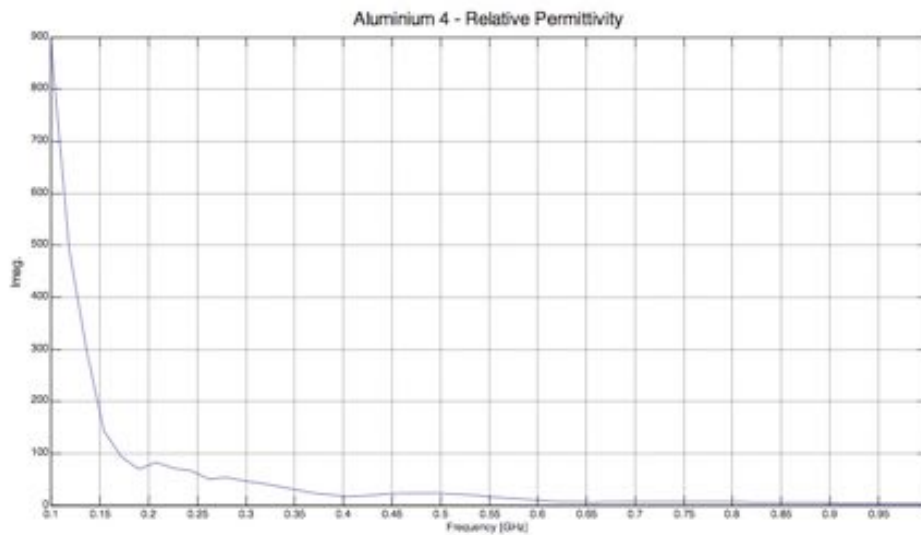
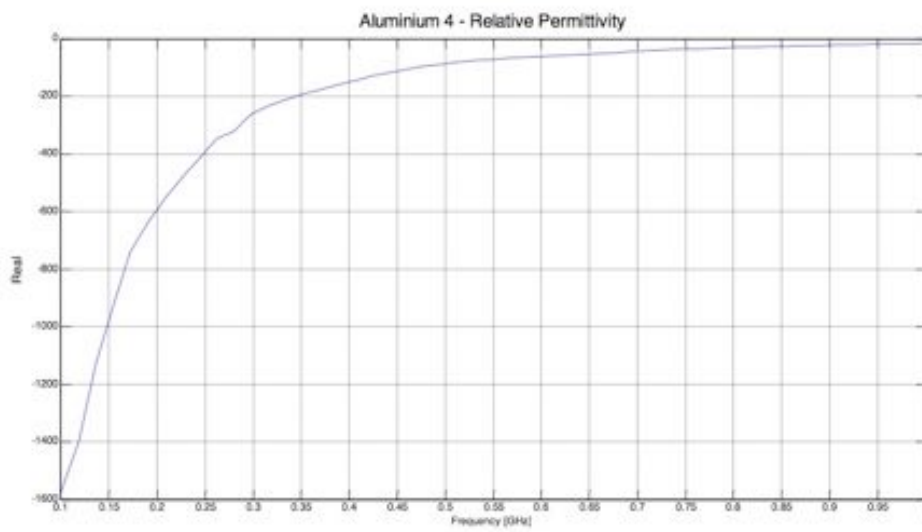
Instead, the permittivity coefficient for the first sample is:

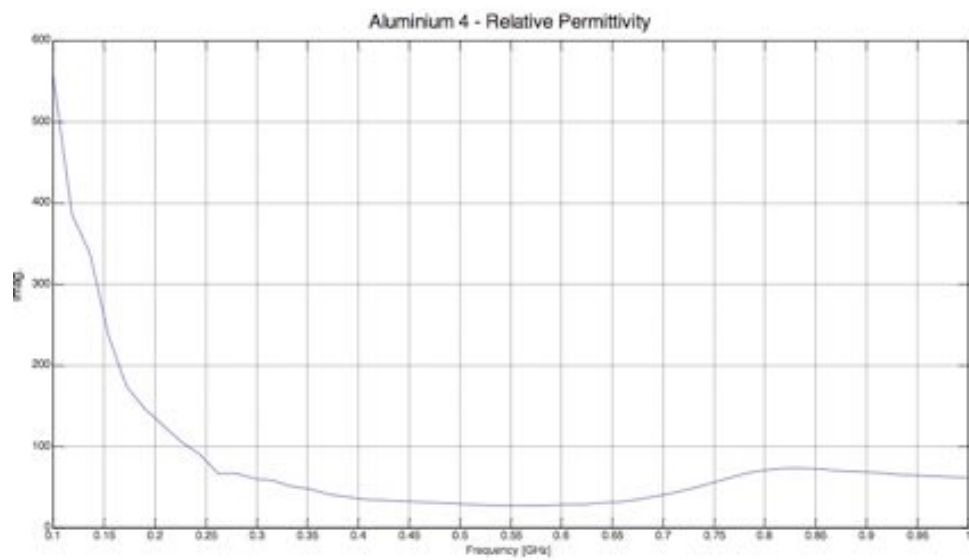
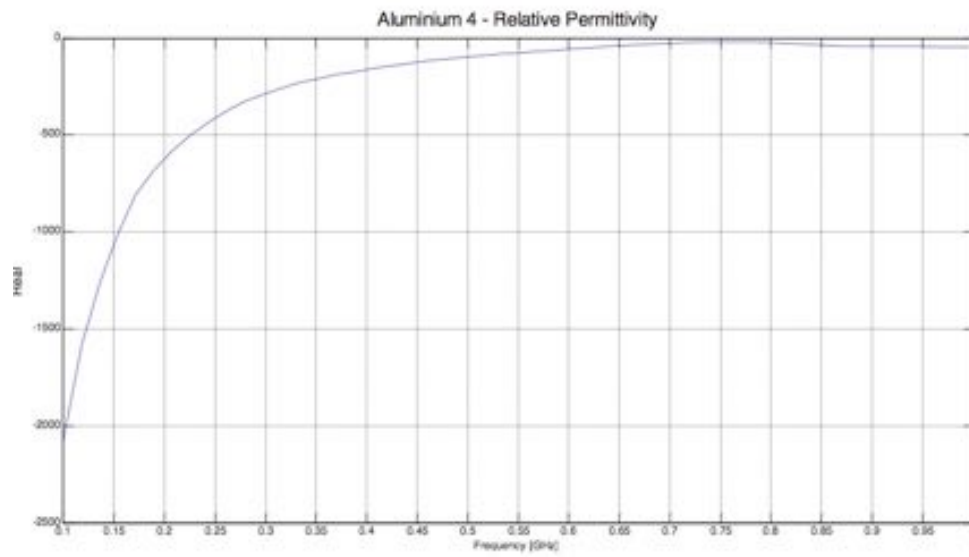
Freq [GHz]	Eps Real	Eps Imag
0.100000	-2080.934814	557.833923
0.118000	-1582.171143	386.017761

0.136000	-1261.921143	336.565582
0.154000	-1006.317688	236.877823
0.172000	-804.719543	174.108124
0.190000	-681.197876	146.717819
0.208000	-581.927551	126.294128
0.226000	-497.292847	105.144005
0.244000	-431.597656	89.734200
0.262000	-373.675690	66.674606
0.280000	-325.799866	66.075073
0.298000	-289.815186	60.464794
0.316000	-258.095551	57.526459
0.334000	-230.215240	50.502510
0.352000	-209.427277	47.187988
0.370000	-189.431030	41.258759
0.388000	-173.146561	37.726654
0.406000	-156.830811	34.817509
0.424000	-142.448441	33.228134
0.442000	-129.558701	32.080051
0.460000	-118.515755	31.002205
0.478000	-108.198433	30.274755
0.496000	-98.739250	29.114479
0.514000	-90.783447	28.290436
0.532000	-82.727188	27.601168
0.550000	-75.594574	27.293530

0.568000	-68.765427	27.157055
0.586000	-62.504864	27.365492
0.604000	-56.325314	27.829348
0.622000	-50.210598	28.659906
0.640000	-43.954254	29.877350
0.658000	-38.051960	31.819859
0.676000	-32.542423	34.726295
0.694000	-27.488783	38.416836
0.712000	-23.296516	43.117897
0.730000	-20.031279	48.740879
0.748000	-18.307476	55.121788
0.766000	-18.875154	61.632057
0.784000	-21.642441	67.105713
0.802000	-25.763172	70.703896
0.820000	-30.254707	72.446381
0.838000	-34.436481	72.612450
0.856000	-37.996086	71.687294
0.874000	-40.881245	70.175293
0.892000	-42.464420	68.670311
0.910000	-43.513084	67.577293
0.928000	-43.923122	65.636559
0.946000	-44.209675	64.544411
0.964000	-44.487270	62.981968
0.982000	-44.872040	62.091316

1.000000	-44.655060	60.931862
----------	------------	-----------





CHAPTER 7

Conclusions

On the basis of the above discussion, some tentative conclusions can be drawn about the possible use of OCMF materials in the beam screens of high synchrotron radiation accelerators.

The outgassing capabilities of OCMF walls can be better by a factor ~ 10 compared to the best slotted walls, and would accordingly allow one to boost the molecular escape probability of beam screens by roughly one order of magnitude, compared to present designs, while keeping the permeable fraction of the beam screen surface unchanged.

The mechanical-structural properties of conducting foams should also be adequate to resist eddy current induced stresses, in view of their morphology. A low SEY is also expected, due to OCMF surface roughness, even though no experimental results are available yet.

The OCMF surface resistance is very low, and almost frequency independent. On the other hand, the (inductive) wall reactance of an OCMF patch is larger by roughly one order of magnitude compared to that of a perforated wall with comparable escape probability.

This drawback could be mitigated by clever placement of the OCMF patches, and/or appropriate reactive loading of the (solid portion of) the pipe wall.

In order to translate the above points into effective design criteria, further modeling effort and substantial experimental work are in order.

Measurement of the complex surface impedance and SEY of metal foams are now underway.

We believe that such an effort is worth being pursued, and that the available modeling tools and technologies provide a good starting point for its successful implementation.

Regarding the measures, we achieve some preliminary results because they are the first on Open Cell Metal Foams' samples. In particular, we can see that, for now, the best candidate is Aluminium 4 foam due to the fact that we have 5 rings of the sample and so the cylinder has a higher thickness.

It seems that this type of foam could have the best characteristics in terms of reflection and transmission coefficients, and so, in terms of permittivity.

In fact, in this particular case, we can consider, for the calculation of the

permittivity, an infinite cylinder.

So we can estimate the permittivity with the known formula, and than, compare the results with the ones that the instrument gives to us with the Nicholson-Ross data reduction.

In the future, there will be a lot of other measurements in order to obtain the wished conclusions and to find important results especially to mitigate the EC phenomenon in high synchrotron particle accelerators.

APPENDIX A

Maxwell's Equations

The equation of motion for a particle of charge e moving under the influence of electric and magnetic fields \vec{E}, \vec{B} is

$$\frac{d\vec{p}}{dt} = e(\vec{E} + \vec{v} \times \vec{B}) \quad (\text{A.1})$$

where $\vec{p} = \gamma m \vec{v}$ is the momentum, \vec{v} is the velocity, and m is the invariant mass. In the expression for the momentum, γ is the Lorentz factor:

$$\gamma = \frac{1}{\sqrt{1 - \frac{v^2}{c^2}}}, \quad (\text{A.2})$$

$$v \equiv \sqrt{\vec{v} \times \vec{v}}. \quad (\text{A.3})$$

The fields must satisfy Maxwell's equations. In a vacuum, Maxwell's equations in differential form are

$$\begin{aligned} \nabla \cdot \vec{E} &= \frac{1}{\epsilon_0} \rho(\vec{r}, t), \\ \nabla \cdot \vec{B} &= 0, \\ \nabla \times \vec{E} &= -\frac{\partial \vec{B}}{\partial t}, \\ \nabla \times \vec{B} &= \mu_0 \vec{j}(\vec{r}, t) + \frac{1}{c^2} \frac{\partial \vec{E}}{\partial t}, \end{aligned} \quad (\text{A.4})$$

where ρ and \vec{j} are the charge and current densities respectively.

Frequently, particularly in simple geometries, the integral forms of Maxwell's equations are more convenient than the differential equations. These are

$$\begin{aligned}
\int \vec{E} \cdot d\vec{S} &= \frac{1}{\epsilon_0} \int \rho dV, \\
\int \vec{B} \cdot d\vec{S} &= 0, \\
\oint \vec{E} \cdot d\vec{l} &= - \int \vec{B} \cdot d\vec{S}, \\
\oint \vec{B} \cdot d\vec{l} &= \mu_0 \int \vec{j} \cdot d\vec{S} + \frac{1}{c^2} \int \dot{\vec{E}} \cdot d\vec{S}.
\end{aligned} \tag{A.5}$$

Here, the line, surface, and volume integrals are connected by the usual conventions. The physical interpretation is more transparent in the integral form. The first is Gauss's Law, a charge q is the source of q/ϵ_0 lines of \vec{E} . The second states that lines of \vec{B} neither begin nor end; that is, there are no free magnetic poles. The third is Faraday's law of electromagnetic induction. The fourth is Ampere's law as modified by Maxwell to include the displacement current contribution. For magnetic materials the last of Maxwell's equations becomes:

$$\nabla \times \vec{H} = \vec{j}(\vec{r}, t) + \epsilon_0 \frac{\partial \vec{E}}{\partial t} \tag{A.6}$$

with \vec{H} and \vec{B} related through the magnetization \vec{M} according to

$$\vec{B} = \mu_0 \vec{H} + \vec{M}. \tag{A.7}$$

In a simple conducting material, the current density is proportional to the electric field, where the constant of proportionality is the conductivity,

$\sigma: \vec{j} = \sigma \vec{E}$. The permeability and permittivity of free space are related through $\mu_0 \epsilon_0 = 1/c^2$, and their values are $\mu_0 = 4\pi \times 10^{-7}$ H/m, $\epsilon_0 = 8,85 \times 10^{-12}$ F/m.

APPENDIX B

The Hamiltonian formalism

For a system with n degrees of freedom, there is a function $H(q,p,t)$ called the Hamiltonian. The variables are n generalized coordinates, their n conjugate momenta, and the time t . The $2n$ equations of motion, *Hamilton's equations*, are then:

$$\dot{p} = -\frac{\partial H}{\partial q}, \quad \dot{q} = \frac{\partial H}{\partial p}. \quad (\text{B.1})$$

The Hamiltonian approach focuses from the outset on motion in the $2n$ -dimensional phase space of the dynamical variables p and q . At the beginning of our discussion, the variables will indeed resemble the momenta and coordinates of elementary mechanism. But that resemblance will fade as we progress. In basic mechanics, we are all familiar with point transformations in configuration space. That is, we introduce new coordinates Q related to the old positions q by n equations of the form $Q=Q(q)$. In phase space, more general transformations among all $2n$ variables are possible and useful. All we require is that the form of Hamilton's equations be preserved.

Suppose we transform from variables p,q to variables P, Q , and that the new Hamiltonian is $K(P,Q,t)$. Hamilton's equations will be valid in both sets of coordinates, provided both satisfy the modified Hamilton's principle:

$$\delta \int (p_i \dot{q}_i - H) dt = 0 \quad (\text{B.2})$$

$$\delta \int (P_i \dot{Q}_i - K) dt = 0 \quad (\text{B.3})$$

where summation over the repeated indices is implied. The “modified” means that both positions and momenta are varied independently between the end points. The above will be satisfied if the integrands differ by only the total time derivative of some function F :

$$(p_i \dot{q}_i - H) = (P_i \dot{Q}_i - K) + \frac{dF}{dt}. \quad (\text{B.4})$$

The transformations that maintain the validity of Hamilton’s equations are called canonical transformations, and F is called the generating function. Note that the modified Hamilton’s principle will remain valid also in the case that the integrands are in the ratio of some constant factor λ :

$$\lambda(p_i \dot{q}_i - H) = P_i \dot{Q}_i - K. \quad (\text{B.5})$$

This is also a canonical transformation, corresponding to a scale change of the variables. The function F is in general a function of both the old and new variables as well as the time. We will restrict ourselves to functions that contain half of the old variables and half of the new; these are useful for determining the explicit form of the transformation. The function F may then take on any of the following four forms:

$$F = F_1(q, Q, t), \quad (\text{B.6})$$

$$F = F_2(q, P, t) - Q_i P_i, \quad (\text{B.7})$$

$$F = F_3(Q, p, t) + q_i p_i, \quad (\text{B.8})$$

$$F = F_4(p, P, t) + q_i p_i - Q_i P_i. \quad (\text{B.9})$$

Now, if we insert each of this into Eq.(B.4), we obtain the relationships between old and new quantities listed below.

$$p = \frac{\partial F_1}{\partial q}, \quad P = -\frac{\partial F_1}{\partial Q}, \quad (\text{B.10})$$

$$p = \frac{\partial F_2}{\partial q}, \quad Q = \frac{\partial F_2}{\partial P}, \quad (\text{B.11})$$

$$q = -\frac{\partial F_3}{\partial p}, \quad P = -\frac{\partial F_3}{\partial Q}, \quad (\text{B.12})$$

$$q = -\frac{\partial F_4}{\partial p}, \quad Q = \frac{\partial F_4}{\partial P}. \quad (\text{B.13})$$

In all four cases,

$$K = H + \frac{\partial F_i}{\partial t}. \quad (\text{B.14})$$

Abbreviations

CERN	European Organization for Nuclear Research
EC	Electron Cloud
HL-LHC	High Luminosity - LHC
L	Luminosity
LHC	Large Hadron Collider
OCMF	Open Cell Metal Foams
PY	Photon Yield
PS	Proton Synchrotron
RF	Radio Frequency
SC	Super Conducting
SEY	Secondary Electron Yield
SR	Synchrotron Radiation

Acknowledgements

Spesso mi soffermo a ripercorrere un po' gli ultimi anni della mia vita, e mi rendo conto quanto tutto sia cambiato, a quanto in realtà io stessa sia cambiata...

Gli anni universitari sono stati duri e impegnativi ma allo stesso tempo ricchi di gratificazioni, e ed ora che sono qui, al culmine del primo importante traguardo, il mio pensiero così come i miei ringraziamenti vanno a coloro che mi hanno accompagnato, sostenuto e supportato in questo intenso viaggio.

Desidero ringraziare, la mia relattrice, la professoressa Stefania Petracca, che mi ha trasmesso la sua stessa passione per la materia che insegna, così come la disponibilità e il premuroso sostegno mostratomi in tutte le fasi dell'elaborazione. È stato un onore e un piacere lavorare con Lei. Non posso non citare il mio correlatore, il professore Arturo Stabile, per il tempo dedicatomi e la pazienza nel chiarire i miei dubbi. Ringrazio tutto il dipartimento di Ingegneria Elettronica dell'università di Salerno, che mi ha ospitata all'interno del proprio laboratorio, il professore Fiumara, mio correlatore e il professore Chiadini i quali mi hanno aiutata e incoraggiata nella mia prima e gratificante esperienza in laboratorio.

Non posso non ringraziare la mia famiglia, in primis mia madre, che anche se non fisicamente, sono certa vegli su di me da lassù, guidandomi nelle scelte importanti della vita dandomi forza quando mi sento persa e nei momenti di sconforto... spero di poterla render fiera di me come oggi, ogni giorno di più.

Ringrazio mio padre che mi ha supportato e sopportato in questi anni universitari con i miei proverbiali sbalzi d'umore e le immancabili crisi esistenziali, papà volevo dirti che ti voglio bene, più di quanto non riesca a dimostrarti.

Alle mie splendide sorelle e a Diego che mi hanno accompagnato negli anni adolescenziali... a mia sorella Eleonora sempre disponibile e pronta a guidarmi con la sua risolutezza e caparbia, a mia sorella Marialaura dolce e materna che si è presa cura di me, e che per me sarà sempre la mia "mamma Aua". Insieme a loro ho affrontato la dura realtà della vita e che, anche se ora sono lontane, non smetterò mai di sentirle vicine e amarle incondizionatamente...

Alla nonna Maria e al nonno Luciano che ci hanno cresciuto, veri esempi di vita e di profuso amore che non dimenticherò mai.

Nonna Rosa, perché anche se ormai sono poche le occasioni di incontro, so di esserci sempre nei suoi pensieri e Nonno Pasquale, perché nonostante la sua austerità riusciva sempre a strapparmi un sorriso.

A Lina e Paolo, che mi hanno accolta come una figlia nella loro famiglia, così splendida e traboccante d'amore.

Un grazie inoltre va a tutti gli amici e colleghi che hanno fatto parte e segnato la mia vita in questi 22 anni, tra cui la neo dottoressa Vera, amica sincera prima che collega con la quale ho avuto il piacere non solo di preparare un gran numero di esami (senza la quale sarebbe stato tutto più difficile) ma anche l'elaborato finale che ci rappresenta e ci ha permesso di rafforzare sempre di più il nostro rapporto. Grazie per tutte le risate, le giornate passate sui libri, grazie per la sincera amicizia mostratami, per la determinazione ma soprattutto grazie per avermi trasmesso tanta grinta in ogni momento di sconforto.

Infine vorrei ringraziare due persone in particolare... me stessa per aver tenuto duro, lottato, pianto, per averci creduto fino in fondo... e in ultimo, non per importanza, il mio impagabile compagno di vita Michele, che senza rumore è entrato nella mia vita, diventandone presto parte integrante, riempiendo ogni momento di dolcezza e profondo amore. Insieme stiamo crescendo e condividendo momenti felici e non... grazie angelo mio... grazie perché ogni giorno non ti stufi mai di sopportare le mie paranoie, le mie crisi, i miei tormenti interiori... grazie per essere sempre lì pronto a consigliarmi e anche a rimproverarmi quando sbaglio... grazie per aver fatto e fare tutt'ora parte della mia vita... anzi di me.

Bibliography

- [1] P.J.Bryant, K.Johnsen, The Principles of Circular Accelerators and Storage Rings, Cambridge University Press.
- [2] D.A. Edwards, M.J. Syphers, An Introduction to the Physics of High Energy Accelerators, J.Wiley , 1993.
- [3] H. Wiedemann, Particle Accelerator Physics I. Springer-Verlag, New York, 1998.
- [4] M. Conti and W.W. McKay, An introduction to the Physics of Particle Accelerators. World Scientific, 1991.
- [5] S.J. Lee, Accelerator Physics (Second Edition).World Scientific, 2004.
- [6] S.Petracca, Electromagnetic fields in Accelerator Pipes from Debye Potentials. October 26, 2004.
- [7] S.Petracca, Coupling Impedances for Complex Multi-Coaxial Accelerator Pipes and Application to LHC. November 17, 1995.
- [8] W. Fischer, M. Blaskiewicz, J.M. Brennan, H. Huang, H.C. Hseuh, V. Ptitsyn, T. Roser, P. Thieberger, D. Trbojevic, J. Wei, S. Y. Zhang, and U. Iriso, Electron cloud observations and cures in the relativistic heavy ion collider. Physical Review Special Topics-Accelerators and Beams, 11(4):041002, 2008.
- [9] M. Pivi, Beam induced electron multipacting in the LHC. PhD thesis, Univ. of Torino, 2000.
- [10] U. Iriso, F. Caspers, J.-M. Laurent, and A. Mostacci, Traveling wave resonant ring for electron cloud studies. Phys. Rev. ST-AB, 7(073501), 2004.
- [11] L. Wang, M. Blaskiewicz, J. Wei, W.T. Weng, K. Ohmi, and R.J. Macek. Mechanism of electron multipacting with a long-bunch proton beam. Phys. Rev., E70(03651), 2004.
- [12] M. Blaskiewicz, M.A. Furman, M. Pivi, and R.J. Macek, Electron cloud instabilities in the Proton Storage Ring and Spallation Neutron Source. PRST-AB, 6(014203), 2003.

- [13] J. Wei and R.J. Macek, Electron cloud effects in high intensity proton accelerators. In Proceedings of ELOUD'02 Workshop, Geneva, April 2002.
- [14] O. Grobner, Beam inducing multipacting. In pp. 3589, Proceedings of PAC'97, Vancouver, 1997.
- [15] O. Grobner. Bunch induced multipacting. In Proceedings of the 10th International Conference on High Energy Accelerators, page 277. USSR Academy of Science, Protvino, 1977.
- [16] K. Harkay and R.A. Rosenberg, Properties of the electron cloud in a high energy positron and electron storage ring. PRST-AB, 6(034402), 2003.
- [17] H. Fukuma, Electron Cloud Observations and Predictions at KEKB, PEP-II and SuperB Factories. Proceedings of ELOUD12: Joint INFN-CERN-EuCARD-AccNet Workshop on Electron-Cloud Effects, La Biodola, Isola d'Elba, Italy, 2012.
- [18] G. Peach, Ionization of atoms and positive ions by electron and proton impact. Journal of Physics B: Atomic and Molecular Physics, 4(12):1670, 1971.
- [19] G. Iadarola, Electron cloud studies for CERN particle accelerators and simulation code development.
- [20] M. E. Rudd, Y. K. Kim, D. H. Madison, and J. W. Gallagher, Electron production in proton collisions: total cross sections. Rev. Mod. Phys., 57: 965 {994, Oct 1985. doi: 10.1103/RevModPhys.57.965.
- [21] J. D. Jackson, Classical electrodynamics. Wiley, New York, NY, 3rd ed. edition, 1999. ISBN 9780471309321.
- [22] A. Hofmann, The Physics of Synchrotron Radiation. Cambridge Monographs on Particle Physics, Nuclear Physics and Cosmology. Cambridge University Press, 2004. ISBN 9781139451109.
- [23] E. Willett, The Basics of Quantum Physics: Understanding the Photoelectric Effect and Line Spectra. The Library of Physics. Rosen Publishing Group, 2004. ISBN 9781404203341.
- [24] R. Cimino, I. R. Collins, M. A. Furman, M. Pivi, F. Ruggiero, G. Rumolo, and F. Zimmermann, Can Low-Energy Electrons Affect High-Energy Physics Accelerators? Phys. Rev. Lett., 93:014801, Jun 2004. doi: 10.1103/PhysRevLett.93.014801.

- [25] A.W. Chao, *Physics of Collective Beam Instabilities in High Energy Accelerators*. Wiley Series in Beam Physics and Accelerator Technology. Wiley, 1993. ISBN 9780471551843.
- [26] L. Tavian, *Performance Limitations of the LHC Cryogenics: 2012 Review and 2015 Outlook*. Proceedings of the Evian 2012 LHC Beam Operation Workshop, Evian, France, 2012.
- [27] R. Cimino and T. Demma, *Electron cloud in accelerators*. International Journal of Modern Physics A, 2014.
- [28] C. Yin Vallgren, G. Arduini, J. Bauche, S. Calatroni, P. Chiggiato, K. Cornelis, P. Costa Pinto, E. M_{etral}, G. Rumolo, E. Shaposhnikova, M. Taborelli, and G. Vandoni, *Amorphous carbon coatings for mitigation of electron cloud in the CERN SPS*. Proceedings of IPAC10, Kyoto, Japan, 2010.
- [29] G. Iadarola and G. Rumolo, *PyECLLOUD and Build Up Simulations at CERN*. Proceedings of ECLLOUD12: Joint INFN-CERN-EuCARD-AccNet Workshop on Electron-Cloud Effects, La Biodola, Isola d'Elba, Italy, 2012.
- [30] U. Iriso, *Electron Clouds in the Relativistic Heavy Ion Collider*. Universitat de Barcelona, 2005.
- [31] S. Petracca and A. Stabile, *Open Cell Conducting Foams for High Synchrotron Radiation Accelerators*. 28 August, 2014. DOI: 10.1103/PhysRevSTAB.17.083503.
- [32] D. Weaire and R. Phelan, *Philos. Mag. Lett.* 69, 107 (1994).
- [33] T. Weiland, *Electron. Commun. (AEU)* 31, 116 (1977).
- [34] H. Zhang, J. Zhang, and H. Zhang, *Smart Mater. Struct.* 15, 759 (2006).
- [35] R. Goodall, L. Weber, and A. Mortensen, *J. Appl. Phys.* 100, 044912 (2006).
- [36] D. A. G. Bruggemann, *Ann. Phys. (N.Y.)* 24, 636 (1935).
- [37] R. McLaughlin, *Int. J. Eng. Sci.* 15, 237 (1977).
- [38] Y. Qui and G. J. Weng, *Int. J. Eng. Sci.* 28, 1121 (1990).
- [39] S. K. Kanaun, *Int. J. Eng. Sci.* 41, 1287 (2003).

[40] T.W. Clyne, in *Comprehensive Composite Materials*(Elsevier, Amsterdam, 2000).

[41] D. Stauffer and A. Aharony, *Introduction to percolation Theory* (Taylor and Francis, London, 1992).

[42] O. Gröbner, *Vacuum* 60, 25 (2001).

[43] S. S. Kurennoy, *Part. Accel.* 39, 1 (1992).

[44] S. Petracca, *Phys. Rev. E* 60, 6030 (1999).

[45] R. L. Gluckstern and B.W. Zotter, CERN Report No. SL96/56 (AP), 1996.

[46] S. Kurennoy, KEK-preprint No. 94-193, 2005.

[47] K. L. F. Bane and G. V. Stupakov, SLAC Pub. 8023,1988.

[48] M. Pivi et al., SLAC Pub. 13020, 2007.

[49] C. Yin Vallgren et al., *Phys. Rev. ST Accel. Beams* 14,071001 (2011).

[50] F. Caspers et al., in *Proceedings of EPAC '02, Paris*(EPS-IGA and CERN, Geneva, 2002), WEPDO031.

[51] R. Cimino, A. Romano, S. Petracca, A. Stabile, M. R. Masullo, S. O'Connor, G Bregliozzi, V. Baglin, in *Proceedings of IPAC '14, Dresden, German, 2013*, WEPME033.